Dynamics of Africa 75 Ma: from plate kinematic reconstructions to intraplate paleo-stresses

Marius C. Wouters[1], Lucía Pérez-Díaz[2,3], Amy Tuck-Martin[2], Graeme Eagles[4], Jürgen Adam[2], and Rob Govers[1]

[1]Tectonophysics Group, Department of Earth Sciences, Utrecht University, P.O. Box 80115, 3508 TC Utrecht, Netherlands
[2]Department of Earth Sciences, Royal Holloway, University of London, TW20 0EX, Egham, Surrey, UK
[3]Department of Earth Sciences, University of Oxford, Oxford, OX1 3AN, UK
[4]Alfred Wegener Institute, Helmholtz Centre for Polar and Marine Research, Am Alten Hafen 26, 27568, Bremerhaven, Germany

Key Points:

- Mechanical equilibrium of the African plate 75 Ma requires slab pull at the Neotethyan convergent zone to be low
- Comparison of modelled intraplate stresses to strain observations supports this result
- Low slab pull points to the absence of a continuous slab, likely due to interference of micro-continents in the closure of the Neotethys

Corresponding author: M. C. Wouters, m.c.wouters@uu.nl

Abstract

Plate reconstruction studies show that the Neotethys Ocean was closing due to convergence of Africa and Eurasia towards the end of the Cretaceous. The period around 75 Ma reflects the onset of continental collision between the two plates, although convergence was still mainly accommodated by subduction, with the Neotethys slab subducting beneath Eurasia. Africa was separated from the rapidly north moving Indian plate by the Owen oceanic transform in the northeast. The rest of the plate was surrounded by mid-ocean ridges. Geologic observations in large basins show that Africa was experiencing continent-wide rifting related to northeast-southwest extension. We aim to quantify the forces and related paleostresses associated with this tectonic setting. To constrain these forces, we use the latest reconstructions of the plate kinematics, while balancing lithospheric body forces, plate boundary forces and the plate's interaction with the underlying mantle. The contribution of dynamic topography to the body forces is accounted for in the model, based on recent publications of reconstructed mantle convective tractions. We model intraplate stresses and compare them with the strain observations. We find that the African plate 75 Ma was mainly driven by slab pull, lithospheric body forces and transform shear tractions. Mechanical equilibrium and the fit to strain observations require the net slab pull, as experienced by the plate, to be unusually low, pointing to the absence of a single continuous Neotethys subduction zone at the time. This corresponds well to reconstructions of micro-continents interfering with the subduction related to the closure of the Neotethys.

1 Introduction

The dynamics of tectonic plates is governed by the interaction of gravity and friction with surrounding plates and the underlying asthenosphere. While models for gravitional forcing on plates, i.e. slab pull and lithospheric body forces, can resolve the magnitudes relatively well (Frank, 1972; Richter & McKenzie, 1978; England & Wortel, 1980; Fleitout & Froidevaux, 1982; Wortel et al., 1991; Meijer & Wortel, 1997; Nijholt et al., 2018), quantification of resistive coupling between plates along different boundary types (Coblentz et al., 1998; Govers & Meijer, 2001; Humphreys & Coblentz, 2007; Van Benthem & Govers, 2010; Warners-Ruckstuhl et al., 2013) and of the tractions on the base of the lithosphere (Forsyth & Uyeda, 1975; Phillips & Bunge, 2005; Conrad & Lithgow-Bertelloni, 2006; Moucha & Forte, 2011; Van Summeren et al., 2012; Flament et al., 2013; Molnar et al., 2015) is not trivial. Tractions on plate contacts govern the first order intraplate stress field (M. L. Zoback, 1992; Heidbach et al., 2010), and are, thus, crucial in the analysis of the deformation in the adjacent plates. Even though the most apparent surface deformation is generally occurring along convergent plate boundaries, tractions on plate boundaries have been shown to produce stresses that propagate through the lithosphere and cause remote intraplate deformation (M. D. Zoback et al., 1993; Xie & Heller, 2009; Cloetingh & Burov, 2011).

Various studies into the evolution of the African plate have tried to link plate kinematic reconstructions directly to observations of tectonic activity (e.g. Janssen et al., 1995; Guiraud & Bosworth, 1997; Guiraud et al., 2005). However, deducing the tractions and corresponding stresses directly from plate kinematics is impossible without a proper description of coupling on plate contacts. Thus, meaningfully linking kinematics directly to geological observations is impossible too. Fortunately, we can constrain traction magnitudes by applying the basic assumption that tectonic plates are in mechanical equilibrium (Forsyth & Uyeda, 1975; Chapple & Tullis, 1977). This torque balance criterion has been previously applied by numerous authors attempting to relate tectonic forces to the kinematics and deformation of various tectonic plates, both for present and past situations: Pacific (Wortel et al., 1991; Stotz et al., 2017, 2018), Juan de Fuca (Govers & Meijer, 2001), South America (Meijer & Wortel, 1992; Stefanick & Jurdy, 1992; Coblentz & Richardson, 1996), Caribbean (Van Benthem & Govers, 2010), Farallon (Wortel & Cloetingh, 1981), North America (Richardson & Reding, 1991), Eurasia (Warners-Ruckstuhl et al., 2013), Africa (Meijer & Wortel, 1999; Stamps et al., 2015), India (Copley et al., 2010) and Australia (Coblentz et al., 1995). The analysis of the African plate by Meijer and Wortel (1999) focused on the correlation between the observations of the Africa-Eurasia collision history and the forces on the rest of the plate, but did not resolve tractions at the northern convergent boundary. Gaina et al. (2013) studied the evolution of African plate boundary lengths, the plate's absolute velocity, and the distribution of oceanic crustal ages since the Jurassic. They also presented paleo-stress models for the plate 68 Ma, but did not constrain their models by torque balance, which is both impairs the reliability of their stresses and the ability to relate their results to tractions on the plate boundaries.

Here, our goal is to determine the distribution of tractions along plate boundaries of the African plate in the Late Cretaceous and their influence on the intraplate stresses and deformation. In addition, we aim to present a rigorous connection between the kinematics and dynamics of the plate and provide a framework for interpreting the relationship between intraplate geological events and lithospheric forces. The nature of the northern plate boundary is a specific point of attention.

Towards the end of the Cretaceous, the African plate was bounded by the convergent Neotethyan boundary in the north, the Owen oceanic transform fault in the northeast and mid-ocean ridges along the rest of the boundaries, as shown in Figure 1 (Seton et al., 2012). The selected 75 Ma, Campanian age, was coeval with the onset of collision following closure of oceanic basins between Africa and Eurasia, which had a large influence on the Cenozoic evolution of the region (Stampfli et al., 2002; Van Hinsbergen et al., 2019). The work presented here is part of a project aiming to constrain the evolution of collision forces in the western Tethyan region. Additionally, the choice for the 75 Ma age is based on the degree of confidence in nature and geometry of Africa's boundaries at the time. Seafloor spreading in the Mascarene basin between India and Africa was well established, while for older ages India was still attached to Africa (Tuck-Martin et al., 2018).

Torque balance cannot constrain the tractions fully to a single unique solution. Therefore, we perform a grid search over the torque balance solution space, to explore the range of possible tractions. In addition, dynamic topography contributions to the lithospheric body forces based on multiple models and two different absolute motion models are considered. For all balanced models in the grid search, the corresponding intraplate stresses are computed. To validate the models we compare the stresses with geological observations. Whilst studies modelling present-day lithosphere dynamics can validate their results against present day stress observations, conveniently compiled in the World Stress Map (Heidbach et al., 2016), we are limited to observations of strain directions associated with historical geological events. Intraplate deformation during the selected time frame was mostly confined to NW-SE trending rifts throughout Africa (Janssen et al., 1995; Guiraud & Bosworth, 1997). In combination with the physical constraints, we constrain the main forces that moved and deformed Africa at the end of the Cretaceous.

2 Tectonic setting

During the Campanian, seafloor spreading around Africa was well established (Figure 1). Seafloor spreading between Africa and South America , which started around 138 Ma between the southernmost parts of the continents, had progressed northward reaching the central Atlantic gateway by 100 Ma (Pérez-Díaz & Eagles, 2014). In the Indian Ocean, divergence between Madagascar and India along the Mascarene basin became established soon after, around 89 Ma (Tuck-Martin et al., 2018). The tectonic situation of the northern convergent boundary was complex (e.g. Stampfli et al., 2002; Van Hinsbergen et al., 2019). Whilst it seems clear that closure of the Neotethys Ocean was being accommo-

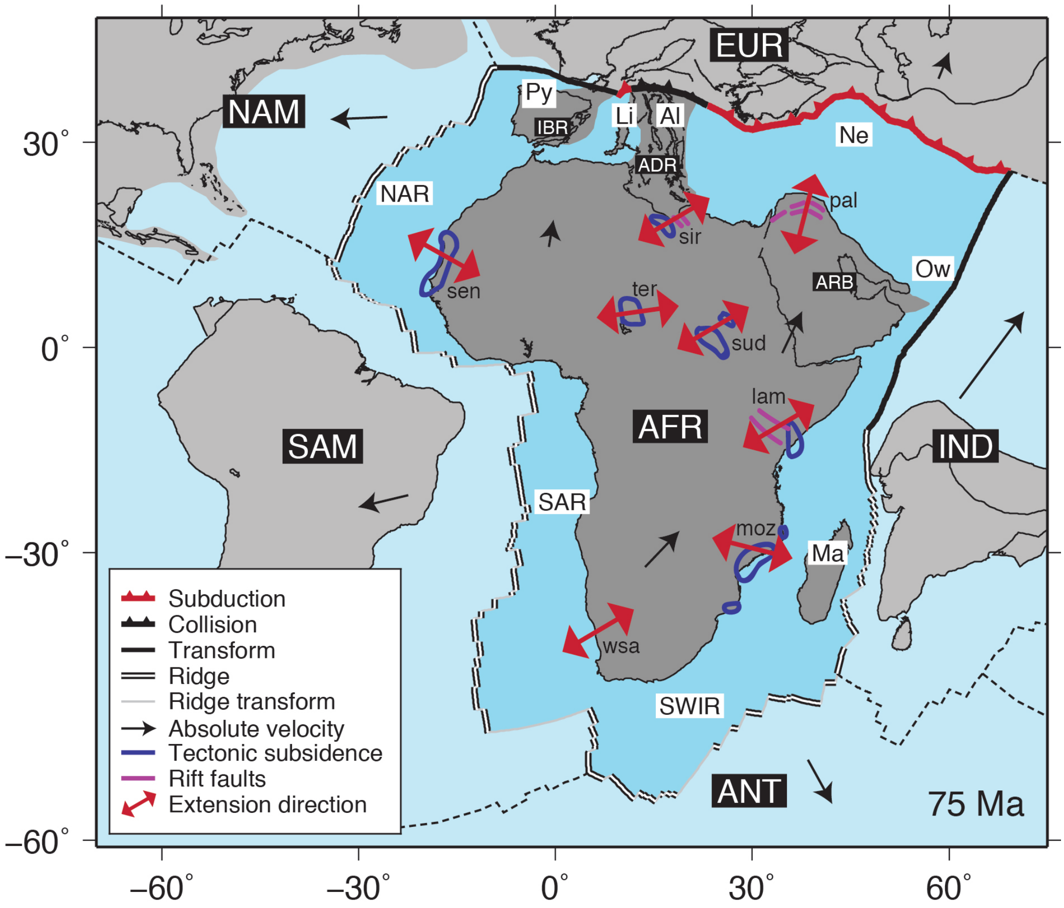

Figure 1. Tectonic setting of the African plate 75 Ma. Locations of geological observations of tectonic subsidence (Janssen et al., 1995), other rift basins with active faults (Abadi et al., 2008; Bosworth & Morley, 1994; Brew et al., 2003) and regional extension (Viola et al., 2012) and their corresponding extension directions are also shown. Plate abbreviations: ADR = Adria, AFR = Africa, ANT = Antarctica, ARB = Arabia, EUR = Europe, IBR = Iberia, IND = India, NAM = North America, SAM = South America. Abbreviations of the plate boundaries: Al = Alpine collision boundary, Ant = Antarctic plate, Eur = Eurasian plate, Ind = Indian plate, Li = Ligurian subduction zone, Ma = Mascarene ridge, N.Am = North American plate, NAR = northern mid-Atlantic ridge, Ne = Neotethys subduction zone, Ow = Owen transform fault, Py = Pyrenees transform fault, S.Am = South American plate, SAR = southern mid-Atlantic ridge, SWIR = southwestern Indian ridge. Abbreviations of rifting locations: lam = Lamu embayment and Anza rift (Kenya), moz = Mozambique basins, pal = Palmyride and Euphrates basins (Syria), wsa = western South African margin, sen = Senegal basin, sir = Sirt basins (Libya), sud = Sudan rifts (South Sudan), ter = Termit trough (eastern Niger). The reconstruction is a compilation of the kinematic reconstructions of SAM-AFR by Pérez-Díaz and Eagles (2014), ANT-AFR and IND-AFR by Tuck-Martin et al. (2018) and EUR-AFR and NAM-AFR by Seton et al. (2012).

dated by some combination of subduction and incipient Alpine collision between the Adria micro-continent(s) and the European plate, the complicating presence of Neotethyan micro-continents means there is no consensus on the geometry and evolution of the plate boundary with Eurasia. The uncertainties in this area stem from the fact that much of the Neotethyan lithosphere has been subducted, and thus information on the past composition has been lost. The simplest reconstruction of the collision is that of Seton et al. (2012), as shown in the northern part of Figure 1. This reconstruction features a large Neotethyan subduction zone, separated from a smaller subduction zone in the Ligurian Ocean, east of Iberia, by a single strip of micro-continent (Adria), which is colliding with Eurasia. More complicated geometries are shown in the reconstructions of Stampfli et al. (2002); Van Hinsbergen et al. (2019).

According to the reconstruction of Seton et al. (2012), relative motion between Eurasia and Iberia, while minor, was occurring along the Pyrenees transform fault (see Figure 2). Arabia was still attached to Africa and would only start separating around 30 Ma as a part of the East African Rift system (Bosworth & Stockli, 2016). The spreading ridge in the Mascarene basin was connected to the Neotethys subduction zone by a long sinistral oceanic transform fault, the Owen transform. This fault is currently still active as the Owen Fracture Zone, accommodating motion between India and Africa, yet the sense of relative motion has reversed with respect to 75 Ma (Gordon & Demets, 1989; Fournier et al., 2011).

Observations of deformation indicate that around 84 Ma (Santonian) Africa experienced an intraplate compressional event, recognised in an overall transition from subsiding basins to folding and the formation of unconformities (Guiraud & Bosworth, 1997; Bosworth et al., 1999). The event has commonly been linked to a shift in relative movement between Africa and Europe, related to a global plate reorganisation, and the onset of Alpine collision (Janssen et al., 1995; Guiraud & Bosworth, 1997; Bosworth et al., 1999; Guiraud et al., 2005).

Faults in rift basins throughout continental Africa were reactivated during the Campanian and Maastrichtian (80-70 Ma). The dominant strike of the affected rifts is NW-SE, indicating a general NE-SW oriented tensional intra-plate stress regime. According to Guiraud and Bosworth (1997) the plate-wide synchronicity of the onset of rifting and the lack of associated volcanism indicates that rifting was not caused by mantle plumes, but instead by the far-field stress effect of plate boundary forces. Janssen et al. (1995) differentiated between rifted basins experiencing thermal and tectonic subsidence, via subsidence rates derived from backstripping analysis. Figure 1 shows a compilation of these tectonically active basins and other active basins not surveyed by Janssen et al. (1995): the Anza rift (Bosworth & Morley, 1994), Palmyride and Euphrates basins (Brew et al., 2003) and an additional part of the Sirt basin (Abadi et al., 2008). Fault slip measurements indicate that the NE-SW extensional regime was also present in western South Africa, although large scale rifting did not develop (Viola et al., 2012).

While describing the rifts, the authors above related them directly to a tensional stress regime and a most tensional horizontal stress (S_{Hmin}) perpendicular to the strike of the rifts. However, stresses are known to preferentially reactivate existing faults (rejuvenation), even in an oblique sense, rather than forming new faults. In addition, evidence for such oblique rifting, e.g. from sets of smaller normal faults in the interior of a rift oriented at an angle to its margins (McClay & White, 1995; Autin et al., 2010), is more difficult to recognize than that for the main normal rift faults, and could, thus, have been overlooked. This imposes an inherent uncertainty on deducing past stress fields from observations.

3 Methods

Our analysis of Africa's dynamics consists of two parts. In the first part, we identify physically realistic sets of tectonic forces that yield mechanical balance of the African plate. In the second part, the balanced force sets are applied to a finite element stress calculation and the resulting stresses are compared with the observations. We focus on the lithospheric averages of horizontal stress, and, likewise, limit our analysis of the tectonic forces to the horizontal components of the forces.

3.1 Torque balance

The forces acting on the plate consist of edge forces, due to the interaction with neighbouring plates, lithospheric body forces, produced by horizontal pressure gradients throughout the plate, and forces at the base of the plate (mantle drag), generated by its interaction with the underlying asthenosphere. In order to obtain mechanical equilibrium the torques on a plate with respect to the centre of the Earth must sum to zero (Forsyth & Uyeda, 1975). For edge forces ($\overline{F}_{E,i}$), mantle drag ($\overline{F}_M$) and lithospheric body forces ($\overline{F}_B$), with their corresponding torques $\overline{T}_{E,i}$, $\overline{T}_M$ and $\overline{T}_B$, the mechanical equilibrium is:

$$\sum_{i=1}^{N_E} \overline{T}_{E,i} + \overline{T}_M + \overline{T}_B = \sum_{i=1}^{N_E} \int_S \overline{r} \times \overline{F}_{E,i}\,\mathrm{d}S \; + \int_A \overline{r} \times \overline{F}_M\,\mathrm{d}A + \int_V \overline{r} \times \overline{F}_B\,\mathrm{d}V \;=\; \overline{0} \qquad (1)$$

where N_E is the number of $\overline{F}_{E,i}$ types, $\overline{r}$ denotes the position vectors of the forces from the centre of the Earth to where they act at the surface, S is the contact area at plate boundary, A the basal area and V the plate volume. The $\overline{F}_E$ terms are divided into types based on the tectonic setting. Although not all force magnitudes are well constrained, their directions ($\hat{f}$) can be estimated using either the relative motion between Africa and the adjacent plates, Africa's absolute motion, or the orientation of the boundary segment, depending on the mechanism. Following Forsyth and Uyeda (1975), the torque balance equation of (1) becomes:

$$\sum_{i=1}^{N_E} F_{E,i} \int_S \overline{r} \times \hat{f}_{E,i}(\overline{r})\,\mathrm{d}S \;+\; F_M \int_A \overline{r} \times \hat{f}_M(\overline{r})\,\mathrm{d}A \;+ \int_V \overline{r} \times \overline{F}_B(\overline{r})\,\mathrm{d}V \;= \sum_{i=1}^{N_E} F_{E,i}\overline{T}^{'}_{E,i} \;+\; F_M \overline{T}^{'}_M \;+\; \overline{T}_B \;=\; \overline{0} \qquad (2)$$

where $\overline{T}^{'}$ is the so-called geometrical torque and F the average force magnitude per unit area of plate contact, i.e. the traction. These F's can be considered the scaling factors of the force directions ($\hat{f}$) and torque directions ($\overline{T}^{'}$). Only positive scaling factors are considered physically realistic, as negative values would, for example, generate resistive forces aiding the relative motion they should be resisting. With this formulation of torque balance, the better known torques are used to solve for the poorly constrained F's.

Plate boundary rheologies are manifested by of both brittle and viscous behaviour, with viscous behaviour mostly occuring in the deeper parts (e.g. Behn et al., 2007). While brittle rheologies are largely invariant to relative velocity on the boundary (Byerlee, 1978), viscous resistance may be somewhat sensitive to relative velocity (Kohlstedt et al., 1995). In modelling the tectonic forces, we assume that the total shear traction along plate boundaries is insensitive to the magnitude of the differential velocity, i.e., that it is mostly controlled by brittle processes.

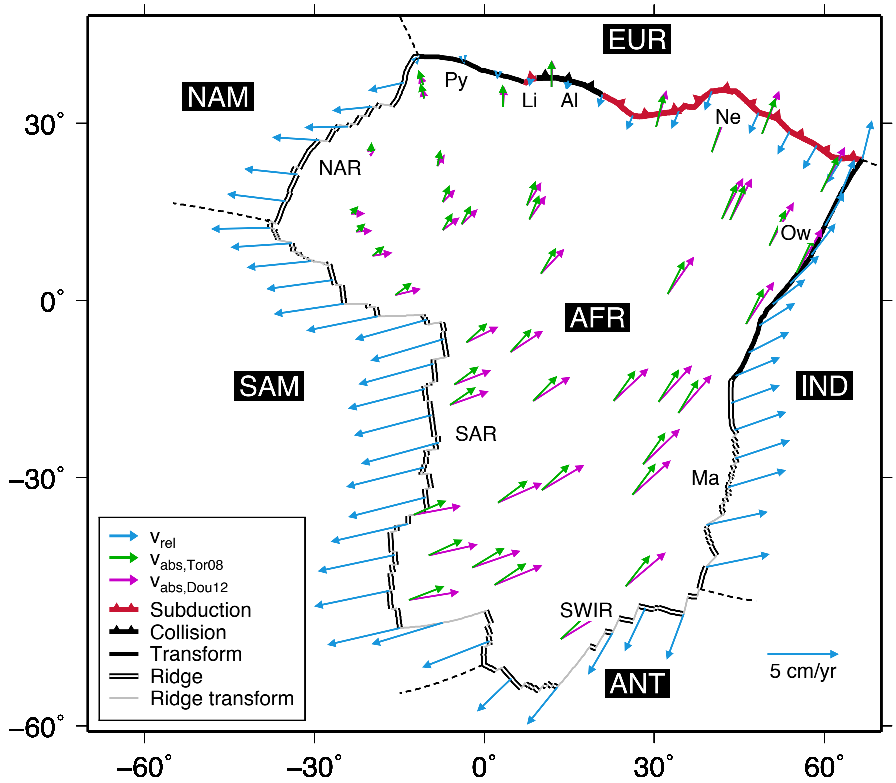

Figure 2. Geometry of African plate boundaries and velocities 75 Ma. Both relative velocities (v_{rel}) of the surrounding plates with respect to Africa from our reconstruction (compiled from Pérez-Díaz and Eagles (2014), Tuck-Martin et al. (2018) and Seton et al. (2012)) and the absolute velocities of Africa with respect to the mantle by Torsvik et al. (2008) and Doubrovine et al. (2012), $v_{abs,Tor08}$ and $v_{abs,Dou12}$, are plotted. Plate boundary abbreviations as in Figure 1.

3.2 Plate reconstructions and kinematics

In our reconstruction of Africa 75 Ma, locations, geometries and types of plate boundaries between Africa and its neighbouring plates are adopted from recent high resolution kinematic reconstructions of SAM-AFR by Pérez-Díaz and Eagles (2014), ANT-AFR and AFR-IND by Tuck-Martin et al. (2018), and EUR-AFR and NAM-AFR by Seton et al. (2012). For the most part determining the plate boundary type is trivial, as Africa was almost completely surrounded by oceanic ridges 75 Ma. However, the tectonic situation along the Neotethyan boundary is more uncertain, with the possibility of a complex interplay of subduction zones and micro-continents between Africa and Eurasia. We follow the relatively simple reconstruction by Seton et al. (2012) for the Neotethyan boundary. According to the work of Seton et al. (2012), there is no relative motion between Iberia and Africa, so we take Iberia to be attached to Africa. In the coming sections we discuss the tectonic forces associated with the various plate boundary types. The reconstructions by Tuck-Martin et al. (2018), Pérez-Díaz and Eagles (2014) and Seton et al. (2012) also provide the basis for mapping oceanic age, which is crucial in order to compute lithospheric body forces and slab pull.

To be able to constrain the directions of the forces ($\hat{f}$), both Africa's absolute velocity and its velocities relative to neighbouring plates are required (Figure 2). The relative velocities in our reconstruction are derived from Pérez-Díaz and Eagles (2014), Tuck-

Martin et al. (2018) and Seton et al. (2012). Because Africa's absolute motion Euler pole is close to the plate, the absolute motion vectors could be particularly sensitive to the exact location of the rotation pole. Therefore, we consider the absolute motions of two different global moving hotspot frames, by Torsvik et al. (2008) and Doubrovine et al. (2012). Both the relative and absolute velocities are displayed in Figure 2.

Some plate reconstructions of the Indian plate feature a double subduction zone between India and Eurasia at the time, as indicated by ophiolites in the Himalayas (e.g. Beck et al., 1996; Corfield et al., 2001) and seismic tomography (Van Der Voo et al., 1999). Stampfli and Borel (2004) also suggested the presence of a mid-ocean ridge between the two subduction zones in their reconstruction. A second subduction zone would effectively decouple the continental part of the Indian plate form the oceanic (Spontang) part in the north. Thus, relative velocities between India and Africa along the Owen transform are uncertain and could have been lower than reconstructed in Seton et al. (2012). However, since our modelled tractions are independent of velocity magnitudes in this study, the implications of the relative velocity uncertainty along the Owen transform are limited.

3.3 Subduction and collision scenarios for the Neotethys plate boundary

A commonly-invoked plate driving force is slab pull ($\overline{F}_{E,sp}$), which is understood as the difference between the total weight of the slab and mantle buoyancy. In the reconstruction by Seton et al. (2012), subduction occurred at the Eurasian margins of the Neotethys and Ligurian oceans (Figure 1). Because our study concerns the deformation and stresses in the surface part of the plate, the slab geometries are not included in the model (Figure 2). The mechanical effect of a slab on the rest of the African plate at the surface is represented by edge forces applied at the trench. These slab pull forces are modelled as acting perpendicular to the trench and are quantified by integration of the slab densities, from the trench to the end of the slab. Thus, the magnitude of slab pull will be strongly dependent on the length of slab attached to the African plate. Despite this, multiple processes could in the complex subduction setting of the Neotethys ocean have led to further variation in the "net slab pull" ($\overline{F}_{E,nsp}$) experienced by the plate. To approach this problem, we initially model a maximum possible slab pull (Figure 3a) before discussing the possible mechanisms that might have reduced the net slab pull (Figure 3b-e).

3.3.1 Finding the maximum slab pull

In modelling the maximum possible slab pull ($\overline{F}_{E,sp}$), a density profile at the trench is constructed from a GDH1 geotherm (Stein & Stein, 1992) associated with the lithospheric age at the trench (Figure 4a). Conductive heating of the slab in the mantle, lowering the density contrast between the slab and surrounding mantle with depth, is also integrated, as described by Wortel et al. (1991) and Govers and Meijer (2001). There are no data on the dip angle of the slabs 75 Ma, but Lallemand et al. (2005) found that the average dip of the deep parts of present-day slabs with a continental overriding plate is $50 \pm 20°$. They found no correlation between slab dip and oceanic age at the trench, but they did identify that slabs tend to dip shallower, up to roughly 15°, if the overriding plate's absolute velocity is towards the subducting plate. Even though Eurasia is shown to be moving away from Africa in the absolute reference frame in Figure 1, the velocity magnitude is small and different absolute motion models show very different absolute velocities for Eurasia 75 Ma (Williams et al., 2015). Because of this uncertainty, we take a conservative approach in the calculating the maximum slab pull by choosing a relatively shallow slab dip of 45°. At shallow depths, where the slab is in contact with the overriding plate, the dip angle tends to be lower. Following the relation between dip angles of shallow and deep parts of slabs by Lallemand et al. (2005), we let the slabs dip at 25° until a depth of 100 km, a rough estimate of the thickness of the Eurasian continental lithosphere.

The maximum slab length is estimated from the consumed oceanic lithosphere in the plate reconstructions of Seton et al. (2012). According to them, continuous subduction of the Neotethys Ocean between Africa (Libya and Egypt) and Eurasia has been reconstructed between its initiation 160-140 Ma and 75 Ma, and is associated with approximately 1300 km of convergence. Between Arabia and Eurasia, the early stages of Neotethyan convergence were complicated by the presence of a third plate between the trench and a Neotethyan mid-ocean ridge just south of it. The ridge progressed north and collided with the subduction zone around 130 Ma, which may have led to a slab breakoff episode (Burkett & Billen, 2010; Pallares et al., 2007). After this, it is clear that more than 2000 km of convergence occurred between Arabia and Eurasia.

The length of subducted Neotethyan oceanic lithosphere is large enough (¿1000 km) for the slab to have reached the transition zone at 670 km, where slabs start to buckle and stagnate above the lower mantle (Fukao et al., 2009; Fukao & Obayashi, 2013). Explanations for this phenomenon range from the buoyancy effects of offset phase transformations within and around slabs to the influence of increased viscosity in the lower mantle (Ito & Sato, 1991; Quinteros et al., 2010; Ballmer et al., 2015; King et al., 2015). Although the exact shape of the viscosity profile across the transition zone is debated (Čížková et al., 2012; King, 2016a, 2016b), most models do exhibit a viscosity increase. Regardless of the reason why, we assume that lower mantle slabs are completely supported and so do not contribute to slab pull, in the same way as Conrad and Lithgow-Bertelloni (2002); Conrad et al. (2004); Goes et al. (2011); Van Summeren et al. (2012). Thus, the slab pull for the Neotethys subduction is modelled to a depth of only 670 km.

The amount of convergence reconstructed by Seton et al. (2012) in the Ligurian Ocean is much smaller: roughly 250 km of oceanic lithosphere was consumed in the subduction zone between 160 and 75 Ma. Given the small dip angle in the shallow parts of slabs, our modelled Ligurian slab only penetrates up to a depth of 100 km, remaining in contact with the overriding lithosphere and thus contributing less to the slab pull.

3.3.2 Mechanisms lowering the net slab pull

With the maximum slab pull modelled ($\overline{F}_{E,sp}$), we next consider the mechanisms capable of reducing the net slab pull ($\overline{F}_{E,nsp}$). One of those mechanisms is mantle resistance to the sinking of the slab (Figure 3b). Although this viscous resistance ($\overline{F}_{E,vr}$) acts on the surface enveloping the slab, we model its overall contribution as an horizontal edge force diametrically opposed to the absolute motion of Africa. Another possible cause for a low $\overline{F}_{E,nsp}$ could be that the slab was shorter (Figure 3c) than reconstructed from Seton et al. (2012). In the light of the potential involvement of micro-continents in the closure of the Neotethys, this seems particularly possible as the entry of mid-ocean ridges or continental lithosphere in subduction zones can lead to slab tearing and breakoff (e.g. Pallares et al., 2007; Wortel & Spakman, 2000). However, subduction of micro-continents could also occur without slab break-off (van Hinsbergen et al., 2005; Capitanio et al., 2010). In intances like this, the buoyancy of the subducting micro-continental lithosphere would counteract the slab pull, hence lowering the net slab pull force (Figure 3d). Alternatively, some reconstructions of the Eurasian collision zone suggest a reversal in the polarity of subduction (Figure 3e, e.g. Stampfli et al., 2002; Van Hinsbergen et al., 2019). A reversal like this would leave no slab attached to Africa, so naturally there would be no net slab pull. Other mechanisms like resistance from phase changes in the upper mantle, corner flow induced by the subduction and bending forces could also contribute to a low net slab pull.

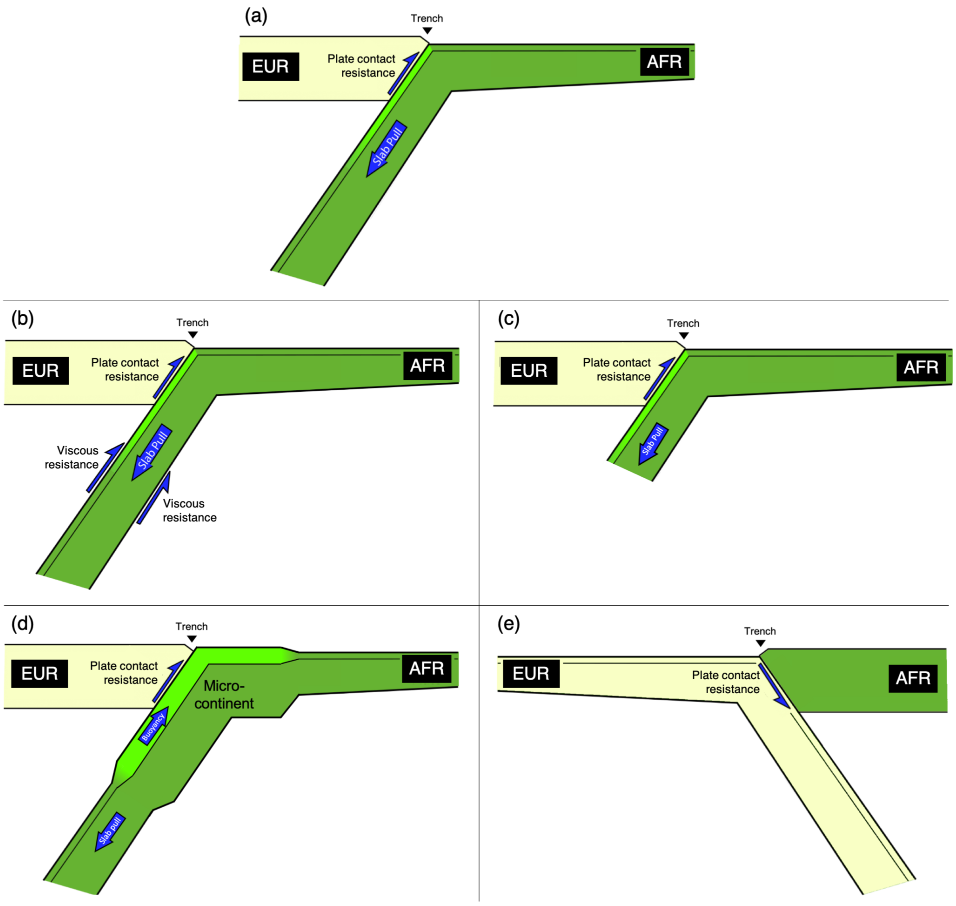

Figure 3. Schematic illustrations of the situation leading to maximum slab pull ($\overline{F}_{E,sp}$) (a) and the mechanisms that might lower the net slab pull ($\overline{F}_{E,nsp}$) (b-e): viscous resistance by the mantle (b), slab breakoff leading to slab shortening (c), subduction of a micro-continent (d) and subduction polarity reversal (e).

Preliminary experiments showed that the torque directions of slab pull ($\overline{T}'_{E,sp}$) and viscous resistance ($\overline{T}'_{E,vr}$) are almost exactly antipodal. Therefore, we consider the viscous resistance as directly resisting the slab pull and incorporate it in the model into the overall net slab pull torque ($\overline{T}_{E,nsp}$). This $\overline{T}_{E,nsp}$ is modelled simply in the direction of the maximum slab pull, with its magnitude scaled back from the magnitude of maximum slab pull ($T_{E,sp}$). The net slab pull magnitude ($T_{E,nsp}$) is constrained by the torque balance. The other mechanisms of Figure 3 also scale back the net slab pull, and are thus indistinguishable from the contribution of viscous resistance in the net slab pull magnitude results.

In addition to the net slab pull, resistance between the slab and overriding plate at the dipping interface between the two plates is also modelled. The direction of this plate contact resistance ($\overline{F}_{E,pcr}$) force is modelled in the same direction as the relative motion at the boundary.

3.4 Transforms

A shear force resists relative plate motion at transform plate boundaries ($\overline{F}_{E,tf}$). We model this transform shear as forces parallel to component of relative motion along the fault. Forces caused by a contractional component of relative motion, transform push forces, are ignored, as these are likely very small, even for cases with a large contractional component (Govers & Meijer, 2001). We also ignore transtensional tractions, because we assume there is no significant transmission of tensional stresses across the transform faults (similar to the decoupling at mid-ocean ridges).

Besides the Owen and Pyrenees transforms, transform faults also link up sections of the mid-ocean ridges (Figure 1). The resistance by these ridge transforms ($\overline{F}_{E,rtf}$) is modelled in the same way as $\overline{F}_{E,tf}$, but we solve the magnitude separately, because the ridge transforms separate younger (Figure 4a), and thus thinner, oceanic lithosphere than the major transforms.

3.5 Continental collision

Collision zones are distinguished from transforms, as the normal component of motion dominates in collision zones. In the case of the Alpine collision as part of our reconstruction, the shear component (Figure 2) is indeed very small (¡0.2 cm/yr). Hence, we only model the compressional normal forces ($\overline{F}_{E,cc}$), as forces in the direction of the normal component of relative motion.

3.6 Lithospheric body forces

Lithospheric body forces (LBFs, $\overline{F}_B$) are produced by the lateral variations of the gravitational potential energy (GPE) (Artyushkov, 1973; Fleitout & Froidevaux, 1982; Rey et al., 2001).The LBFs are computed as the negative of the gradient of the modelled GPE field (Figure 5). The LBFs include, and are completely consistent with, ridge push forces (Richter & McKenzie, 1978), passive margin forces (Sandiford & Coblentz, 1994), and forces associated with crustal thickness variations (Frank, 1972; Artyushkov, 1973).

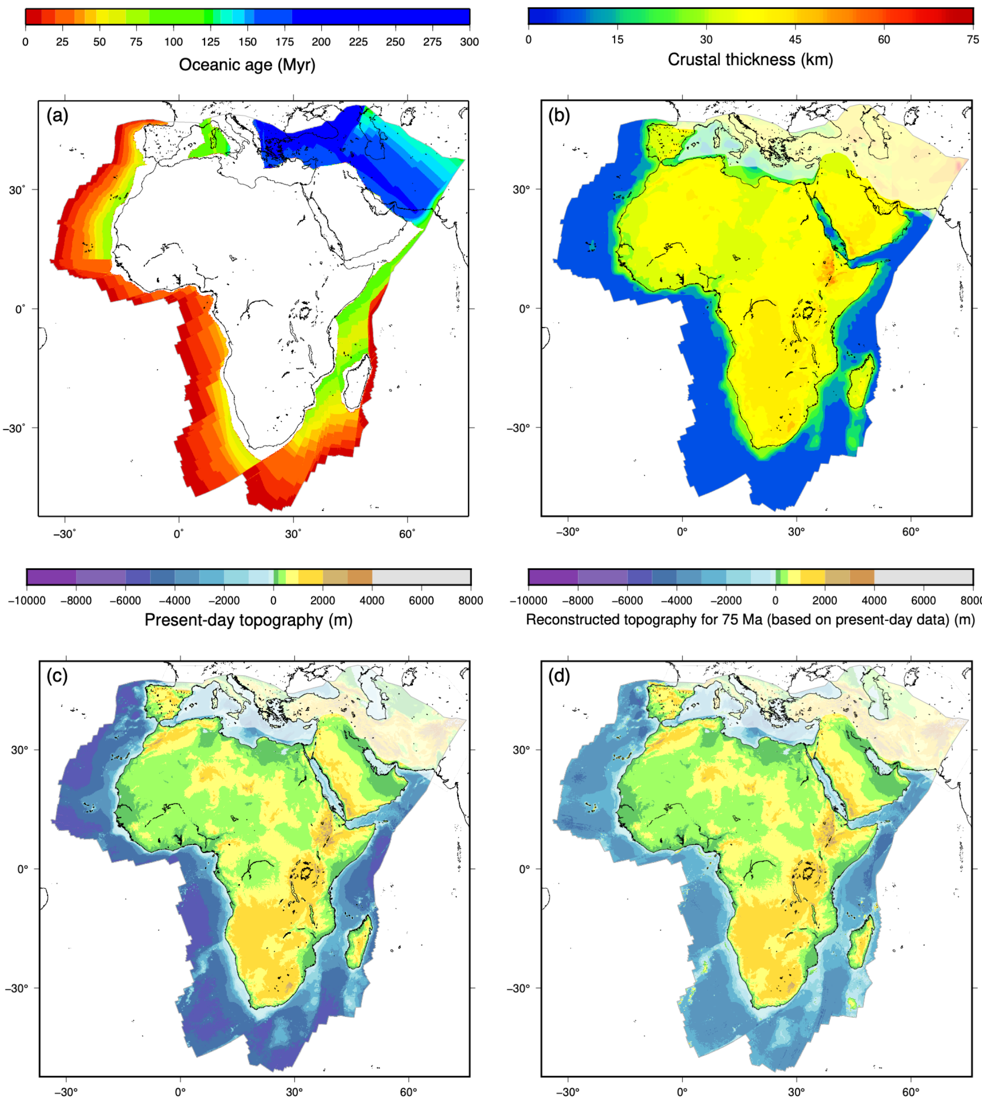

Figure 4. Data sets for the calculation of the slab pull forces (a) and the GPE field (a-d). All are plotted with Africa fixed in its present-day position. (a) Ages of the oceanic lithosphere at 75 Ma. The age distribution is a compilation of age grids by Pérez-Díaz and Eagles (2017), Seton et al. (2012) and the age distribution derived from the kinematic model of Tuck-Martin et al. (2018). (b) Present-day crustal thickness map derived from Globig et al. (2016) for the African and Arabian continents and from CRUST1.0 (Laske et al., 2013) for rest of the continents and the oceanic parts. (c) Present-day topography and bathymetry of GEBCO_2014 (Weatherall et al., 2015) (d) As Figure 4c, but the reconstructed subsidence between 75 Ma and now is subtracted from the bathymetry. The light shaded areas on the crustal thickness and topography maps indicate the uncertain Neotethys area where the present-day data strongly differ from the 75 Ma situation.

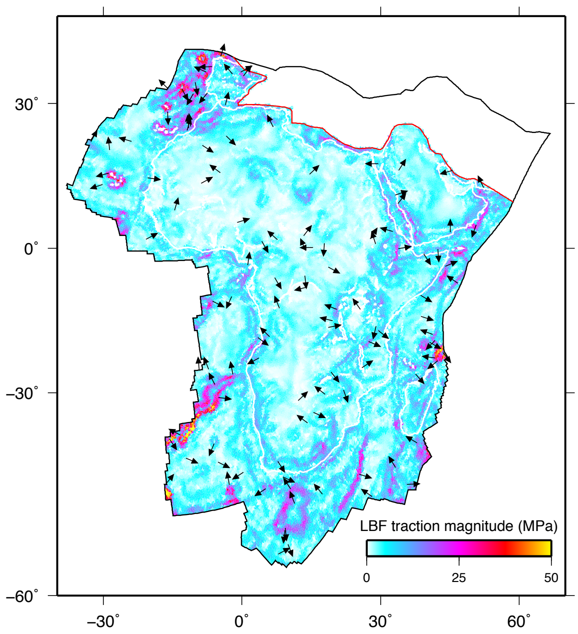

Figure 5. Distribution of the LBF tractions in the 75 Ma paleo geographical coordinates. A selection of traction directions is represented by black arrows. We exclude the Neotethyan tractions due to the large uncertainty in the GPE field there. Present-day coastlines rotated to the 75 Ma frame are shown in white. A low-pass filter with a lower bound at 100 km is applied to the LBF traction data.

The calculation of the GPE field is based on the assumption of lithospheric isostasy, as by Nijholt et al. (2018) and Warners-Ruckstuhl et al. (2012), with the addition of modelling the influence of dynamic topography on the GPE too. For the isostatic part of the calculation, the density and pressure distribution in the lithosphere is constructed by balancing the crustal thickness and topography variations with a variable density of the lithospheric mantle. Loading by the water column above both continental and oceanic lithosphere is also included. The isostatic compensation depth is taken to be at the base of the reference continental lithosphere. Thickness of the oceanic lithosphere is approximated from the oceanic ages (Figure 4a) using the GDH1 cooling model (Stein & Stein, 1992), with asthenosphere underlying the oceanic lithosphere. The transitions from thinned continental to oceanic lithosphere are based on the plate reconstructions of Figure 4a. Densities of the water, crust and asthenosphere layers are assumed to be constant at 1000, 2850 and 3200 kg/m^3. We refer to the supporting information of Nijholt et al. (2018) for details on the GPE computation.

Since data on the crustal thickness distribution is unavailable for 75 Ma Africa, we are restricted to present-day observations (Figure 4a). Crustal thicknesses of the African and Arabian continents are from Globig et al. (2016), who used elevation and geoid data and seismic observations. For the remaining continental and oceanic crust, thicknesses are from the CRUST1.0 model (Laske et al., 2013), based on seismic and gravity data, with statistical averages of crustal thickness for unsampled regions.

Topography and bathymetry are also required, and again, we are mostly limited to present-day observations (Figure 4c), using the digital elevation model of GEBCO_2014 (Weatherall et al., 2015). In addition, the of amount of oceanic subsidence during the

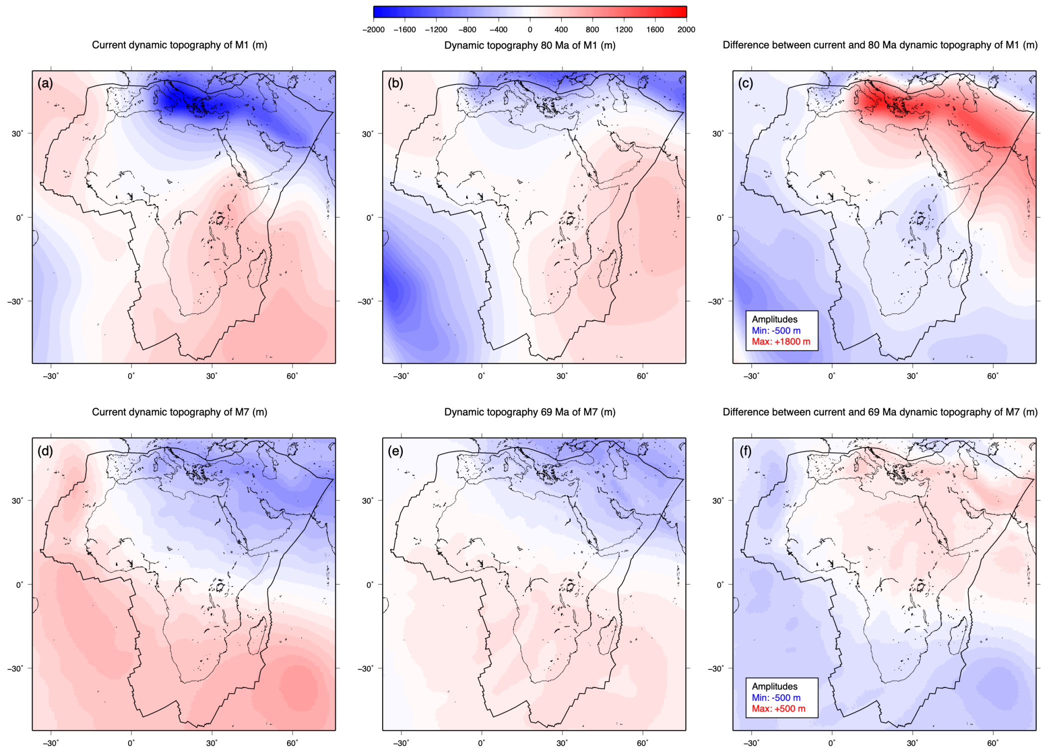

Figure 6. Dynamic topography models used in the calculation of the LBFs, in the frame with Africa in its present-day position: model M1 (a-b) and model M7 (d-e), both from Müller et al. (2018). The differences between current and historic dynamic topography are plotted adjacently (c,f). The maximum and minimum amplitudes in the differential fields are also given.

75 Myr between the studied age and the data is approximated with the oceanic cooling model GDH1 (Stein & Stein, 1992) and the oceanic ages of Figure 4a. The reconstructed bathymetry, with the subsidence removed, is displayed in Figure 4d.

As mentioned before, a major challenge in modelling the tectonic forces on the African plate 75 Ma stems from the uncertainty regarding the exact shape and type of the African plate's northern boundary in the Neotethys. This makes constraining crustal thickness and topography of the area practically impossible, as indicated by the light shaded areas in Figure 4b-d. Because of this uncertainty, we did not model LBFs for Neotethys (see blank area of Figure 5). A cautionary test using present-day topography and crustal thickness suggested the overall torque ($\overline{T}_B$) should be relatively unaffected by this omission. However, it does have an effect on the reliability of the modelled local stresses, since the situation of zero LBF tractions is unrealistic.

3.6.1 Effect of dynamic topography

The radial component of mantle flow causes dynamical support of the lithosphere, termed dynamic topography, which changes the pressure at the lithospheric compensation depth. Since the dynamic topography changes over time and it alters the GPE field, we expand our isostatic GPE calculation for the dynamic topography, to arrive at lithospheric body forces which incorporate the influence of dynamic topography ($\mathrm{LBF}_{\mathrm{DT}}$).

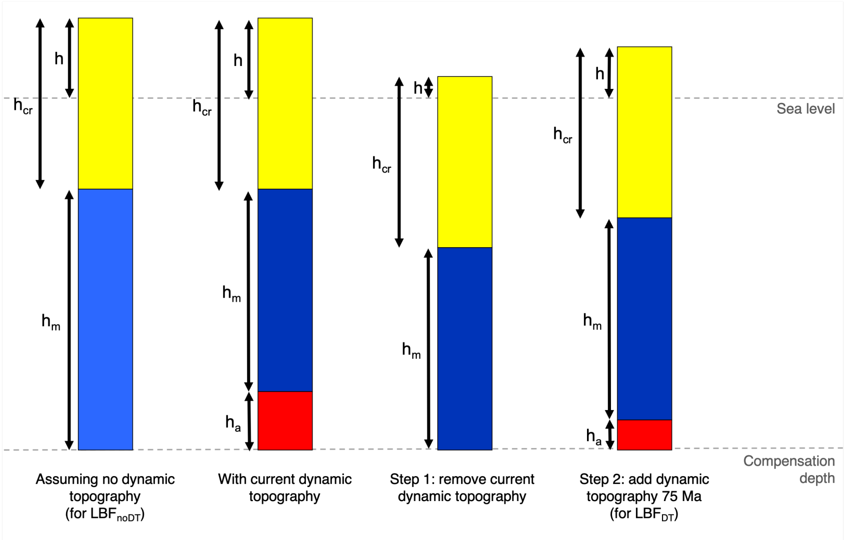

Figure 7. Schematic illustrations of the isostatic columns for the steps of the GPE calculation with consideration of dynamic topography (Figure 6). Here h, h_{cr}, h_m and h_a stand for topography, crustal thickness, thickness of the lithospheric mantle and the thickness of asthenosphere above the compensation depth (dynamic topography). The first column shows an apparent isostatic situation of thickened continent given data on the h and h_{cr} (Figure 4b,d) and the assumption of no dynamic topography, as it is used in the calculation of Nijholt et al. (2018). In reality, the h_m is different (here smaller) due to dynamic topography, introducing a column of asthenospheric mantle to our formulation of isostasy, whose presence requires the density of h_m to differ too (as indicated by the brightness change). To compute the GPE field 75 Ma with dynamic topography we apply a two step approach. In the first step, the present-day dynamic topography is removed and the corresponding GPE of this column is calculated in the purely isostatic way from Nijholt et al. (2018). Then, the dynamic topography 75 Ma and its corresponding asthenospheric contribution (h_a) is added. In this example, the dynamic topography is positive both for the present-day and 75 Ma situation, but the calculation is the same for other combinations of dynamic topography signals. Similarly, although thickened continent is shown here, the calculation steps are the same for thinned continent and oceanic parts, with their corresponding isostatic calculations following Nijholt et al. (2018).

Models of present and past dynamic topography have been made using different methods, from forward models of mantle convection driven by plate motions and slabs to models backward advecting mantle densities from tomography to hybrids of the two (Flament et al., 2013). However, there is only limited agreement between the modelled dynamic topography and observed residual topography, both in terms of the pattern and the amplitude of the topography, with in general long wavelength structure being over-estimated and small wavelengths underestimated (Hoggard et al., 2016; Müller et al., 2018; Cowie & Kusznir, 2018; Davies et al., 2019). In our choice for the dynamic topography reconstruction to apply, we follow the work by Müller et al. (2018), who evaluated multiple reconstructions by comparing the predictions of continental flooding to geological data on paleo-coastlines. We choose to implement two of their dynamic topography models that appear to correspond well in terms of land fraction and spatial overlap (Figure 6): M1, the hybrid backward and forward model from Spasojevic and Gurnis (2012) and M7, a modification of the forward model by Barnett-Moore et al. (2017). Neither models includes a time slice at exactly 75 Ma, so we use their time frames of 80 Ma and 69 Ma from M1 and M7, respectively.

The calculation steps for the GPE including the effect of dynamic topography are displayed in Figure 7. We first remove present-day dynamic topography and calculate the GPE of that column isostatically, and then add the GPE contribution of the dynamic topography 75 Ma to it. The resulting GPE field is rotated to Africa's position of 75 Ma and LBFs are computed. So, since we consider both present-day and historic dynamic topography, the difference between them (Figures 6c,f) will dictate the magnitude of the effect the dynamic topography has on the LBFs. The pattern of the differential fields are mostly comparable, however, the amplitudes of M1 ($\sim$1150 m) are significantly larger than those of M7 ($\sim$500 m).

We do recognise that the adopted models (Figure 6) likely overestimate dynamic topography amplitude at long wavelengths (Müller et al., 2018) and that the overall LBF torque is mostly sensitive to the same long wavelengths in GPE. To take account of this, we allow the amplitude of the dynamic topography used in the GPE calculation to scale back when solving torque balance. We also consider the lithospheric body forces in the case where dynamic topography amplitudes are scaled down to zero ($\mathrm{LBF}_{\mathrm{noDT}}$), i.e. the case where we assume no dynamic topography of Figure 7.

Present-day small scale topographic features (e.g. erosional peaks and valleys) are most likely to have been formed between 75 Ma and the present. Features on this scale tend to symmetrical, and so should not contribute significantly to the overall GPE torque. We remove their influence, by applying a low-pass filter to the GPE traction field. The low-pass filter applied excludes wavelengths smaller than 100 km. The influence of the choice of low-pass filter cutoff is explored in section 5.3.

3.7 Basal drag

Basal drag ($\overline{F}_M$) is the force that arises from the horizontal component of asthenospheric traction on the base of the lithosphere. A hypothetical stationary asthenosphere would induce a passive mantle drag antiparallel to the absolute velocity of the plate. However, the mantle is not stationary and for some plates the interaction between convective mantle flow and the lithosphere (active drag) has actually been shown to be a requirement for torque balance (e.g. the Eurasian (Warners-Ruckstuhl et al., 2010) and Pacific (Stotz et al., 2018) plates). Dominance of either passive or active mantle drag is essentially governed by the interplay between mantle motion and the absolute motion of the plate, and could well be different for each plate.

Stamps et al. (2015) found that for the present-day African plate Couette-type asthenospheric flow, which is solely induced by shear from plate motions, leads to a better fit to observed plate velocities than Poiseuille-type flow, which is flow imposed by mantle convection models. In this concept of Couette flow the shear tractions are almost identical to our simple passive drag formulation. Therefore, and because reconstructed asthenospheric flow for 75 Ma is even more uncertain than present-day flow, we apply just the passive drag in the torque balance. If the results show the requirement for active drag in the torque balance, we can reconsider our decision to disregard it.

3.8 Exploring the solution space

In solving the torque magnitudes via the torque balance, only 3 scaling factors in equation 2 can be constrained. However, our model has more than three unknown parameters (scaling factors and model choices), as only the magnitude of torque of lithospheric body forces without dynamic topography ($\mathrm{LBF_{noDT}}$ is already constrained). So, we employ a grid sampling of the solution space, the full range of parameters sets that satisfies torque balance. The complete solution space is 9 dimensional: the scaling factors $F_{E,nsp}$, $F_{E,pcr}$, $F_{E,tf}$, $F_{E,rtf}$, $F_{E,cc}$, F_M, the choice between the two dynamic topography models of Figure 6, the scaling of the dynamic topography amplitudes in those models and the choice between the two absolute motion models. We solve for $F_{E,pcr}$, $F_{E,tf}$ and $F_{E,cc}$ with the torque balance, so employ the grid sampling to the remaining 6 dimensions. To ensure that we sample the solution space fully, we first perform tests of the approximate extent of the parameter ranges resulting in balance, and then choose the sampling ranges broadly around. Here, we exclude negative scaling factors (F's) as these would lead to unrealistic (i.e. driving) directions for the resistive tractions.

3.9 Intraplate stress modelling

To obtain the stress response of the force sets obeying torque balance, they are applied as discrete boundary conditions in solving the mechanical equilibrium equations with the GTECTON finite element code (Govers & Meijer, 2001). Computation occurs on a spherical shell using the formulation of plane stress and is fully elastic, with a Young's modulus of 100 MPa and a Poisson's ratio of 0.3, as averages for both the crustal and mantle part of the oceanic and continental lithosphere. The shell has a uniform thickness of 100 km, an estimate for the average lithospheric thickness, as oceanic and continental lithosphere are on average 75 $\pm$31 km and 134 $\pm$64 km (Steinberger & Becker, 2018). Since stresses acting on a plate are more dispersed in thicker than in thinner lithosphere, the shell thickness governs the stress magnitudes. Similarly, variations in lithospheric thickness, from cratons to other continental to oceanic lithosphere , will influence the stress magnitudes. However, we only have stress direction observations, not the magnitudes, when comparing the models to the observations, so that accounting for lithospheric thickness variations to accurately model stress magnitudes is of limited importance.

We adopt an irregular triangular finite element grid containing 92,206 elements. Displacement gradients resulting from the tectonic forces are converted into stress via the Young's modulus and Poisson's ratio. To ensure that the overall displacement and rotation of the domain is constrained, two anchor nodes are selected in the grid. Because these stationary nodes can cause artificial stress concentrations in the surrounding stress field, we perform pilot experiments to carefully choose the locations for the anchors where the displacement of the solution is already low, limiting the magnitude of the artifacts.

Elastic behavior captures the short term response of rocks to tractions. It, thus, serves as the potential for permanent geological deformation by brittle and viscous mechanisms on a longer term. We assume that away from major faults, on the spatial scales of the plate, the rheology will be roughly isotropic, so that stress is directly related to strain. In reality, relaxation of stress, be it either viscous in shear zones or by brittle slip on faults, can cause deviations of the stress orientations. When dealing with stress observations around major faults or shear zones, these deviations are important. However, we only have observations of the major rifts themselves and are interested in how well our imposed stresses can explain the presence of large scale extension there, so we are not concerned with the exact deviation of stresses locally. Potential oblique rifting is considered in the design of our misfit function (see section 3.10 and Appendix A). Overall, we see the purely elastic rheology as a justifiable simplification of the lithospheric rheology for our purpose of evaluating the force models with the observations of rifting.

3.10 Fitting to observations

We evaluate the parameter sets by comparing the modelled stresses to the geological observations (Figure 1), in order to find the parameter values resulting in the best fitting models. The geological observations of rifting contain information on both the stress regime (normal) and the orientation of stress (S_{Hmin} perpendicular to the rifts). However, as discussed above, a component of oblique reactivation can be expected. We incorporate this observational uncertainty into the design of our misfit function (ϕ). We choose to be conservative in considering the strike-slip regime and an azimuthal discrepancy of 45° to represent the boundaries between good and bad fit. For details on the design of the misfit function, see Appendix A. To obtain the fit of single parameters values (p), we compute the marginal probabilities ($P(p)$), using a simplified version of the approach by Nijholt (2019):

$$P(p) = \sum_{m=1}^{N_p} e^{-\frac{1}{2}\phi_m^2} \tag{3}$$

summing over the fits of all the balanced models that contain the particular parameter value (N_p). In order to consider the fit of a combination of parameters (p_1, p_2), we compute the 2D marginal probabilities:

$$P(p_1, p_2) = \sum_{m=1}^{N_{p_1,p_2}} e^{-\frac{1}{2}\phi_m^2} \tag{4}$$

where N_{p_1,p_2} is the number of balanced models that contain both p_1 and p_2.

4 Results

4.1 Models resulting in torque balance

The geometrical torques ($\overline{T}^{'}$) in equation (2) are computed from force directions ($\hat{f}$). Intersections between Earth's surface and positive ends of the torque vectors are displayed in Figure 8. There appear to be two clusters of torques, which we categorize as either the driving or resisting torques, based on their proximity to the absolute motion poles. The LBF torques happen to be in roughly the same direction as the absolute plate motion, thus they are seen as driving the plate. Therefore, in this case of Africa 75 Ma, the LBFs and slab pull were both driving the plate roughly north. The LBF torques that include the influence of dynamic topography ($\mathrm{LBF_{DT}}$) deviate from the torque without dynamic topography influence ($\mathrm{LBF_{noDT}}$), especially for the M1 model of Müller et al. (2018). As the torque of the transform shear traction is close to the absolute Euler pole (forces acting in roughly the same directions as the absolute motion), we choose to categorise the torque as driving. The driving nature of the transform forces in this case can also be recognised in Figure 2, with the relative motion along the Owen transform fault being in the direction of Africa's absolute motion. In other words, the shear tractions from the fast moving Indian plate were dragging Africa northward 75 Ma.

The driving $\overline{T}'_{E,sp}$, $\overline{T}'_{E,tf}$ and $\overline{T}'_{B}$ are resisted by plate contact resistance at the subduction zone ($\overline{T}'_{\underline{E},sp}$), passive mantle drag ($\overline{T}'_{E,dr}$), ridge transforms ($\overline{T}'_{E,rtf}$) and continental collision ($\overline{T}'_{E,cc}$). The overlap between the gray area spanned by resisting torques

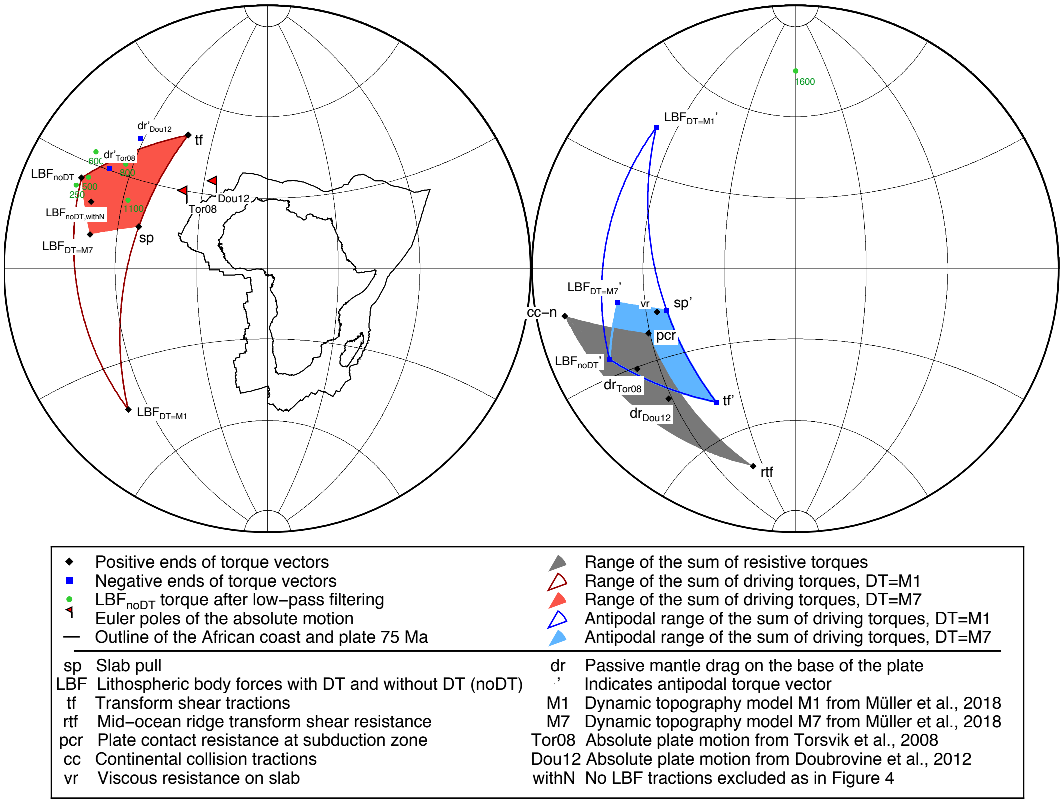

Figure 8. Torques acting on the African plate 75 Ma. The torques are categorized either as driving (red) or resisting (gray) torques to aid the interpretation of torque balance, as described in the text. The torque directions of both the LBFs with and without the effect of dynamic topography (see Figure 7) are shown. As the dynamic topography amplitudes are scaled down, the influence of dynamic topography decreases and the $\mathrm{LBF_{DT}}$ torques move in the direction of the $\mathrm{LBF_{noDT}}$ torque. The effects of low-pass filtering the $\mathrm{LBF_{noDT}}$ torque are illustrated for cutoff wavelengths of 250, 500, 600, 800, 1100 and 1600 km (green dots). The low-pass filtering cutoff for $\mathrm{LBF_{noDT}}$ as used in the main analysis is at 100 km.

and the blue area spanned by antipodal driving torques in Figure 8 shows that torque balance is possible (Warners-Ruckstuhl et al., 2010).

The overlap contains the complete solution space of the torque balance. The results of a grid sampling of this solution space are displayed in Figure 9. Of the 345,092 sets tested, 9,330 show torque balance. The scaling of edge force magnitudes (TN/m) is converted to approximate tractions using the cross sectional length (L) of the assumed simplified plate contact geometries of Table 1.

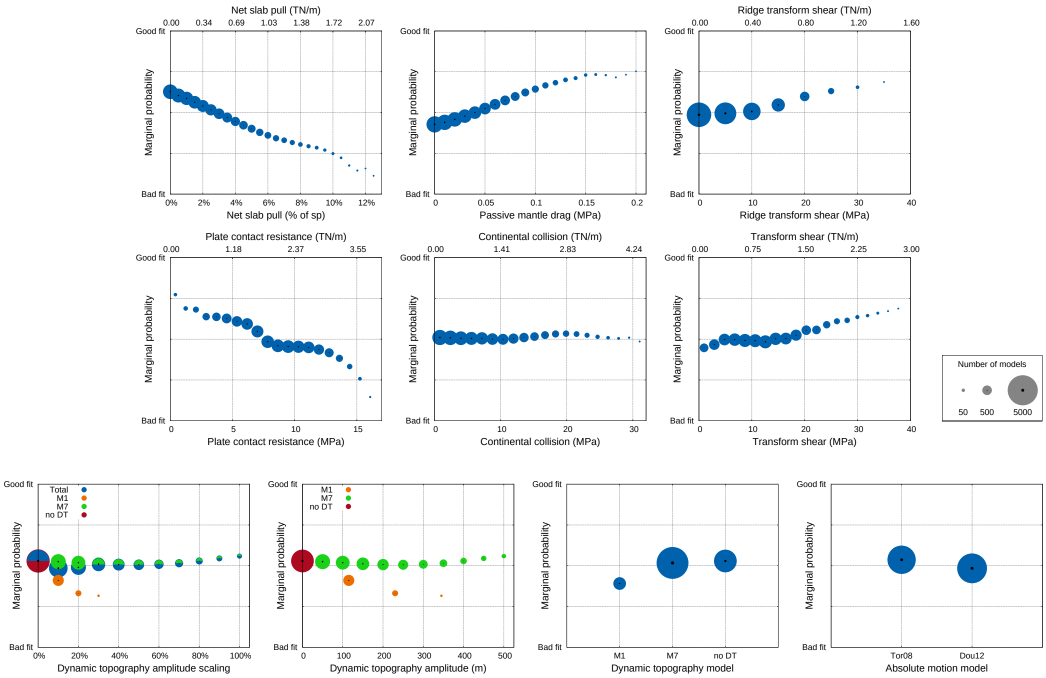

Figure 9. Marginal probabilities, as described in Appendix A, for the parameters investigated in the grid sampling. Symbol size indicates the distribution of models throughout the ranges, i.e. the number of models obeying torque balance for a given value. The edge force magnitudes (TN/m) are converted to tractions (MPa) using the cross sectional length (L) of the assumed simplified plate contact geometries of Table 1. For the dynamic topography scaling, the probability distributions of both dynamic topography models are also plotted. To see how the scaling relates to the absolute amplitudes, the approximate dynamic topography amplitudes are plotted alongside too. M1 and M7 are dynamic topography models by Müller et al. (2018) and Tor08 and Dou12 are moving hotspot frames by Torsvik et al. (2008) and Doubrovine et al. (2012).

For passive mantle drag and the edge forces, a broad range of tractions is possible, yet the distribution of models showing balance is not uniform throughout the range, as evident from the variable symbol size. In addition, both absolute motion models and dynamic topography models lead to balanced sets. When using the M1 dynamic topography model (Figure 6a-c), balance is only possible if the dynamic topography amplitudes are scaled down significantly, to 30% or less, which corresponds to maximum amplitudes of approximately 350 m or less. For the M7 model (Figure 6d-f), balance is possible regardless of the amplitude scaling. Overall, most balanced model sets include low amplitude dynamic topography. The most noteworthy result is that of the net slab pull, which has to be $\leq$12.5% of maximum slab pull magnitude. This indicates the presence of strong mechanisms opposing or reducing slab pull.

4.2 Fit to observations

The solution space of possible force sets leads to a range of possible stress fields (see Figure 10a). For the majority of locations, fit between the modelled stresses and observations is possible. The Senegal basin, Palmyride and Euphrates basins, and the western South African margin show a poor fit. The fit is especially poor for the Palmyride and Euphrates basins, which lie close to the region of removed LBF tractions (Figure 5).

Table 1. Simplified contact geometries corresponding to the different boundary types. The surface areas of the contacts are approximated using estimates for the depth extent of the contact (D), the dip angle of the contact (α) and the resulting cross sectional length perpendicular to the boundary (L). The D values are taken from the averages of lithospheric thicknesses for different tectonic regimes from Steinberger and Becker (2018): orogenic continent for continental collision and plate contact at the subduction zones, intermediate age ocean for transform boundaries and young ocean for ridge transform boundaries.

	Contact geometry		
Plate contact type	D (km)	α (°)	L (km)
Continental collision	100	45	141
Plate contact at subduction zone	100	25	236
Transform	75	90	75
Ridge transform	40	90	40

Comparisons between modelled stress directions and the observations are used to identify best fitting models inside this range (details on the fit in Appendix A), and, thus, to identify the most likely parameter values (Figure 9). This analysis reinforces the torque balance result of low net slab pull, as the modelled stresses fit best if net slab pull goes to zero. Other parameter estimates are also advanced by the comparison to observations: high tractions for passive mantle drag, transform shear resistance and ridge transform resistance produce best fits, albeit representing only a small portion of the total number of models. Low values for plate contact resistance fit best. There is a slightly better fit when using the absolute motion of Torsvik et al. (2008) than that of Doubrovine et al. (2012). Using the M7 model by Müller et al. (2018) in the calculation of the dynamic topography component of the LBFs, results in better fits than using the M1 model. While the fit degrades with increasing dynamic topography amplitude for M1, the probability distribution for the M7 amplitude scaling is roughly flat. This is also the case for continental collision resistance and indicates that the modelled stresses are insensitive to the exact values of these two parameters, i.e. they cannot be constrained beyond the torque balance result.

The two dimensional marginal probabilities are shown in Figure 11a. They give an impression of the complex shape of the multidimensional torque balance solution space. They can also show possible parameter dependencies. Contour lines aid the identification of the dependencies, which should cause diagonal contours. However, pairs of independent parameters that both have a strong slope in the one dimensional marginals (Figure 9) could lead to similarly diagonal contours, as the best fits would be located in one of the corners of the plot. Thus, we only consider the pairs of parameters exhibiting an internal diagonal pattern as certainly interdependent. In Figure 11, such patterns are clearest between mantle drag and continental collision, between mantle drag and plate contact resistance and between transform resistance and ridge transform resistance, where the former two pairs are anticorrelated and the latter is correlated. Both anticorrelations are between parameters related to resistive torques, while the correlated pair relate to one driving (tf) and one resistive (rtf) torque.

4.3 Best fitting models

The marginal probabilities of Figures 9 and 11a display the sensitivities of the modelled stresses to the different parameters and show which parameters values generally produce the best fits. However, simply selecting the parameter values with the higher marginal

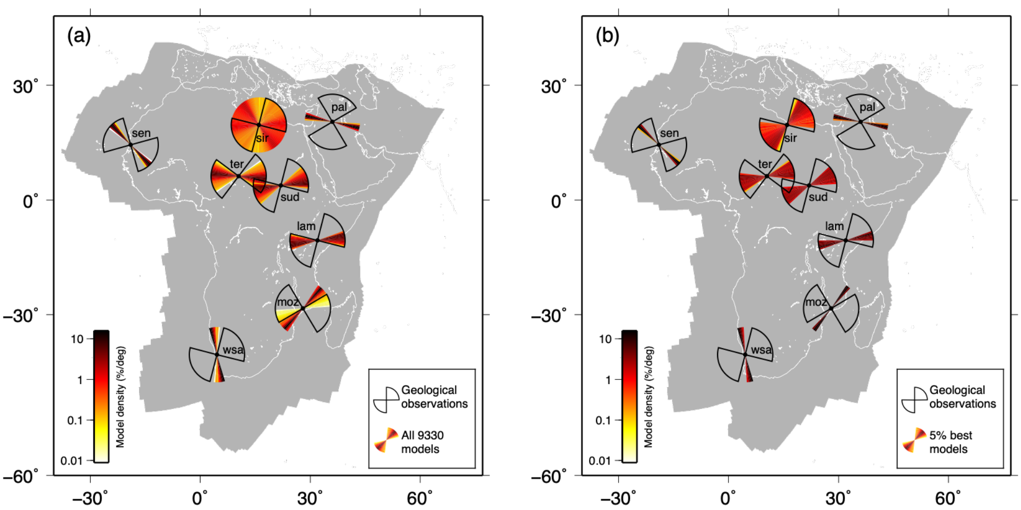

Figure 10. Comparison between modelled and observed S_{Hmin} directions for all modeled stress fields (a) and for only the 5% best fitting models (b). The S_{Hmin} directions from geological observations are plotted as wedges to account for the observational uncertainty in stress direction. For each location the range of modelled S_{Hmin} directions is also plotted as wedges, with the wedges coloured according to the model density. The model density represents the percentage of the total number of models per degree, so that most models line up in the dark coloured directions.

probabilities does not necessarily lead to the identification of one overall best fitting model. In our case, a model chosen this way does not even show torque balance.

To get a better image of the characteristics of the high-scoring models, we explore the subset of the 5% best fitting models (466 models). The stress orientations of this subset naturally exhibit a better fit (Figure 10), with obvious improvements the locations that already showed a good fit. The fits of remaining locations remain poor. The two dimensional probabilities of the best 5% are displayed in Figure 11b. They show the smaller ranges of parameters associated with the best models. These ranges (Table 2), indeed do not all align with results of the marginal probabilities: where Figure 9 indicates that the magnitudes of mantle drag, transform and ridge transform resistance should be large for good fits, the best 5% of models comprise of a wide range of values, indicating an insensitivity of the fit to these parameters. Other parameters do show higher sensitivity, as only a portion of the full torque balance range is included in the range of the subset of best fitting models. These are net slab pull, plate contact resistance, continental collision and dynamic topography scaling. All of them are relatively small for the best fitting models, with values of $\leq$4%, $\leq$7.6 MPa, $\leq$16 MPa and $\leq$60%.

The marginal probabilities of Figure 11b also show clearer parameter dependencies. We identify correlations of transform resistance with ridge transform resistance and, possibly, with plate contact resistance and anticorrelations of mantle drag with the dynamic topography amplitude scaling, continental collision resistance, transform resistance and, possibly, with ridge transform resistance.

In order to show both a representation of the stress fields associated with models that fit the observations well and the variability between those stress fields, stresses from two of the 5% best fitting models are plotted in Figure 12. We choose to display the model that scores absolute best and the model that scores worst of the 5% best fitting mod-

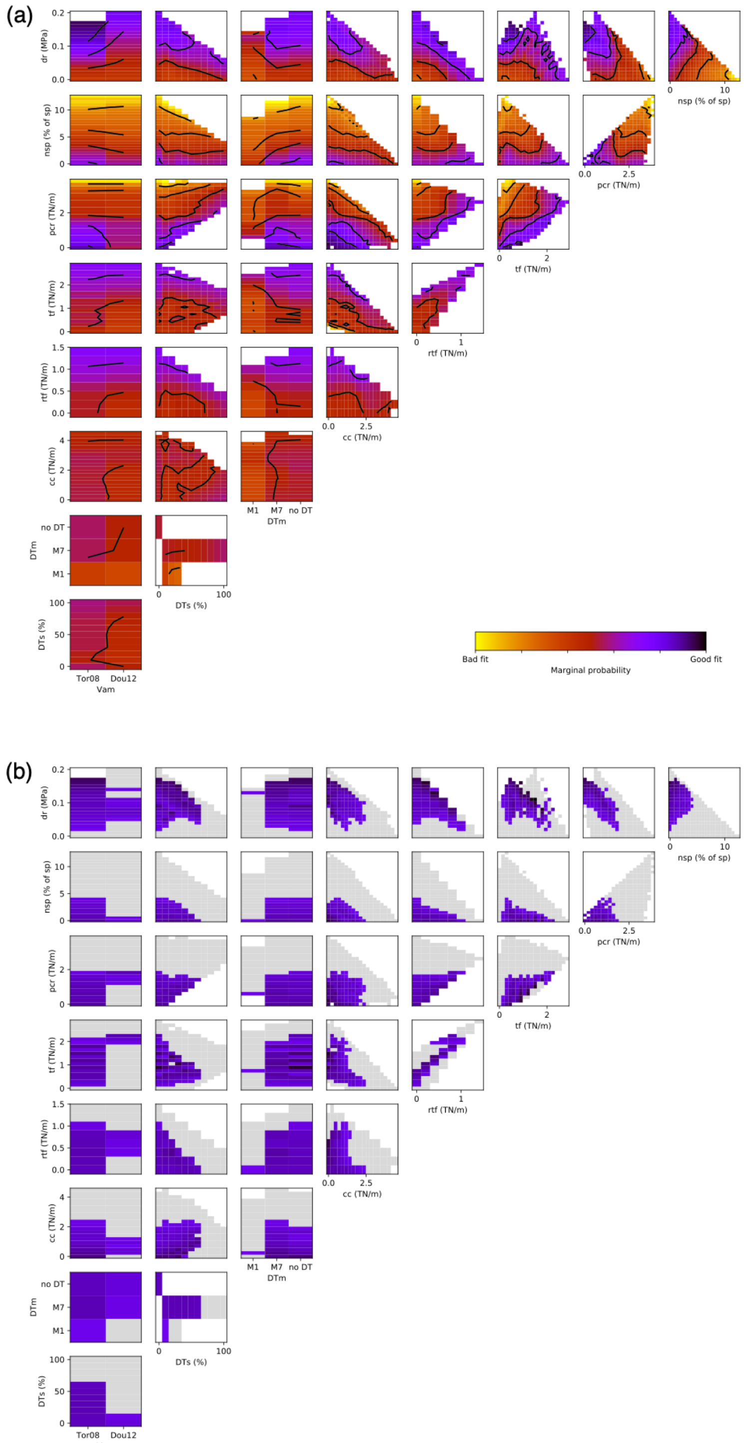

Figure 11. 2D marginal probabilities for the parameters investigated in the grid search. Probabilities are plotted for all models (a), with contour lines to aid the identification of parameter dependencies, and for the best 5% of the models (b). Plots of (b) use the same color bar as (a) and the distribution of all models is plotted behind in gray. Abbreviations of the parameters are the same as in Figure 8, with the addition of the absolute motion model (Vam), the dynamic topography model (DTm) and dynamic topography amplitude scaling (DTs).

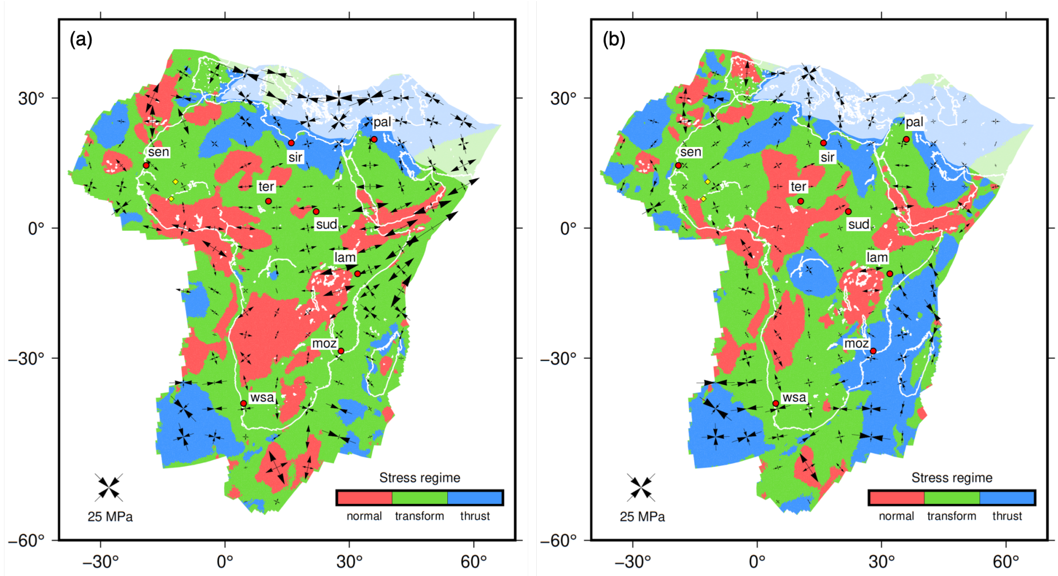

Figure 12. Modelled stresses for the African plate 75 Ma for the model that is ranked 1st (a) and the model ranked 466th (b) out of all 9330 models. Arrows represent the principal horizontal stresses and colours show the distribution of the stress regimes. Red dots denote the locations of rifting observations and yellow diamonds the locations of the anchor points used in the modelling.

els, i.e. the models ranked 1st and 466th. The parameter values for these two models are given in Table 2. An obvious difference between the models is the magnitude of the transform resistance traction (20.4 versus 3.3 MPa). The large transform resistance is expressed in the stress field of Figure 12a by the large stress magnitudes along the Owen transform fault. Rather than demonstrating how the specific combination of parameters contributes to the good fit of the rank 1 model, this illustrates how the fit between the observations and stresses are insensitive to certain parameters, like the transform resistance. In general the orientations of stresses and the pattern of stress regimes, with normal regimes mostly in continental parts, is comparable between the two models. The magnitudes of the stress, however, differ substantially between them, illustrating the overall insensitivity of our model to stress magnitude. This is not surprising, since our fit to observations is only based on stress orientation and regime, not magnitude.

5 Discussion

5.1 Cause of the low net slab pull

In order to achieve torque balance on the plate, the net slab pull ($F_{E,nsp}$) needs to amount to 12.5% or less of the maximum slab pull ($F_{E,sp}$) (Figure 9a). For the 5% best fitting models, our $\frac{F_{E,nsp}}{F_{E,sp}}$ ratio is actually $\leq$4%. When compared with other studies (Table 3), despite their lack of clear consensus, it is clear that our result of $\leq$4% is exceptionally low. As discussed in section 3.3.2, there are multiple possible mechanisms that can lower the net slab pull. We deem it to be unlikely that this exceptionally low value is solely caused by a strong resistance of the mantle as in Figure 3b. In the light of the complex geometry of micro-continents interacting with the subduction as reconstructed by Stampfli and Borel (2004) and Van Hinsbergen et al. (2019), additional mechanisms like those in Figure 3c-e need to be considered. Identifying which of the mechanisms were occurring at the time is beyond the aims of this study. What is clear though

Table 2. Parameter values of the two models selected from the 5% best models, which are both displayed in Figure 12, and the full ranges of the parameter values of the 5% best models (Figure 11b).

Model rank	nsp(%)	dr(MPa)	pcr(MPa)	tf(MPa)	rtf(MPa)	cc(MPa)	DTm	DTs(%)	DTs(m)	Vam
1	0	0.11	4.0	20.4	15	0.1	-	0	0	Tor08
466	1.5	0.08	3.3	3.3	0	12.7	M7	20	100	Tor08
Range										
Min	0	0.02	0.02	1.5	0	0.02	M1	0	0	Tor08
Max	4	0.17	7.6	30	25	16	M7	60	300	Dou12

Table 3. Compilation of studies that have modelled net slab pull compared with this study.

Study	Description	$\frac{F_{E,nsp}}{F_{E,sp}}$
Becker et al. (2001)	Analogue subduction model	>90%
Schellart (2004)	Analogue subduction model	8-12%
Conrad and Lithgow-Bertelloni (2002)	Fitting absolute motions globally	>70%
Capitanio et al. (2009)	Numerical slab model	38-82%
Wortel et al. (1991)	Pacific plate dynamics	∼30%
Govers and Meijer (2001)	Juan de Fuca plate dynamics	70-90%
This study	African plate dynamics	≤12.5%
	Fit with stresses	≤4%

is that it is unlikely that there was long, continuous north-dipping Neotethys slab attached to Africa as reconstructed in Seton et al. (2012).

5.2 Torques driving absolute motion

At any point in time, the forces on a plate govern its absolute motion. More specifically, all the torques of forces that can influence the absolute motion direction combined ($\overline{T}^*$) should align in the same direction as the absolute motion pole. This obviously includes the driving torques, as defined in section 4.1, but torques from resisting forces can also influence the direction of a plate's motion. For example, resistive shear tractions between neighbouring plates, like the ridge transform tractions in our case, can introduce an additional rotational component to the plate motion in all cases except where those forces are aligned exactly in opposition to the absolute velocity. Similarly, the inward facing forces produced by collision can also cause rotation. This possibility excludes only the passive mantle drag, which simply reacts to the absolute motion. Because of torque balance, we know that $\overline{T}^*$ as the combination of all torques except mantle drag, should have the exact antipodal direction to the mantle drag torque.

The antipodal mantle drag torques plotted in Figure 8, however, show that the directions of $\overline{T}^*$ do not exactly match their corresponding Euler poles of absolute motion. This could indicate the presence of an active mantle drag component, which alters the the mantle drag torque direction. Despite this, because the best 5% of models seem to be relatively insensitive to the magnitude of mantle drag (Figure 11b), as evident from the wide range of magnitude values in the 5% best subset, we deem it unlikely that a small deviation of the mantle drag torque direction would significantly influence our results for the other forces.

5.3 Lithospheric body force uncertainties

Uncertainties in the calculation of the GPE field arise from the lack of data of the past topography and crustal thickness, with the largest uncertainties around the northern Neotethys boundary. Figure 8 shows that the influence of this area on the overall LBF torque appears to be small, as is evident from the minor deviation of the LBF torque which includes the LBF tractions in the northern boundary ($\mathrm{LBF}_{\mathrm{noDT,withN}}$) from the one where this area is excluded ($\mathrm{LBF}_{\mathrm{noDT}}$) as in Figure 5. Even though the overall torque seems to be relatively insensitive to the uncertainty in the Neotethys area, using appropriate paleotopography and paleo crustal thicknesses would be preferred to properly resolve the stresses regionally. This could reduce the misfit of stresses close to the Neotethyan margin, at the Palmyride and Euphrates basins (Figure 10). For a large part of the rest of the plate the use of present-day topography and crustal thicknesses is defensible as

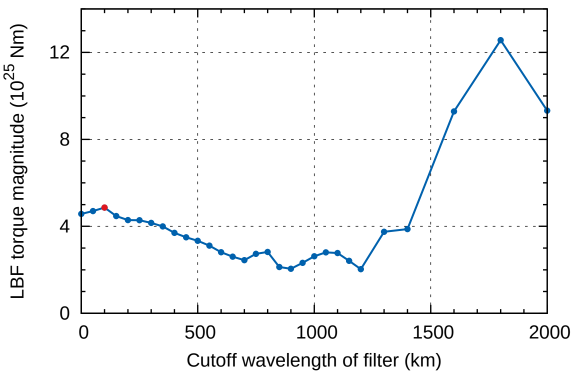

Figure 13. Influence of filtering short wavelength LBF tractions (all wavelengths smaller than the cutoff wavelength) on the corresponding overall LBF torque magnitude. The red dot indicates the preferred filtering, used to calculate LBF tractions in the main analysis.

the African continent has been relatively stable between 75 Ma and now and a correction for the subsidence in the oceanic parts is applied. The East African and Red Sea rifts, which started forming only since 30 Ma, could be a significant influence on the body forces and stresses, although, part of the effect of their presence is already corrected for using dynamic topography.

To further explore the sensitivity of the body forces to uncertainties in the input data, we have performed a test on the influences of different wavelengths of topography and crustal thickness. In our results so far, wavelengths in the LBF traction field smaller than 100 km are eliminated with a low-pass filter (Figure 5). In the test we vary the cutoff wavelength of the filter, ignoring progressively longer and longer wavelengths of the LBFs. Both the LBF torque magnitudes in Figure 13 and LBF torque directions in Figure 8, indicate that the LBF torque is relatively unaffected by wavelengths of 250 km and smaller. Filtering wavelengths larger than 500 km from the LBF traction field causes the torques to deviate significantly, both in magnitude and orientation.

Even though the LBF torque magnitude and direction appear to be insensitive to short wavelength topography, small scale topography could still be important for the eventual stress field pattern. However the stress fields display only minor differences between a case without filtering and one where wavelengths smaller than 250 km are removed. This shows that uncertainties in small scale features do not propagate to the stresses. The results indicate that for future studies aiming to reconstruct paleo-topography for Africa with the intent to calculate LBFs, resolving topographic features smaller than 250-500 km will be unnecessary.

6 Conclusions

The tectonic forcing on the African plate 75 Ma was a balance between slab pull, lithospheric body forces and transform shear resistance against the continental collision, plate contact resistance at subduction, ridge transform resistance and mantle drag forces (Figure 8). The transform traction from the fast-moving Indian plate also contributed to drive African plate motion.

The intra-plate stress orientations and regimes best match the strain observations when the net slab pull is very low, at ≤4% of the maximum possible slab pull. In addition, small magnitudes of plate contact resistance at the subduction zones (≤7.6 MPa) and continent collision tractions ($\leq$16 MPa) result in the best fits (Table 2). The fit to observations is relatively insensitive to the traction magnitudes of mantle drag, transform resistance and ridge transform resistance, as evident from their wide range of values associated with the best 5% of models (Figure 11b).

The net slab pull value of $\leq$4% is exceptionally weak in comparison to other studies. This indicates that there likely was no continuous north-dipping Neotethys slab 75 Ma. Instead, the Neotethyan convergent zone was likely more complex owing to the involvement of micro-continents, with possibly shorter slabs, which may have led to slab detachment, subduction polarity reversal or even continental subduction (Figure 3). Best fits to observations are achieved when the dynamic topography amplitudes are relatively low, at 300 m or less.

Topography and crustal thickness variations on spatial scales smaller than 250-500 km contribute to local stress variations, but not to the overall plate dynamics.

Appendix A Functions for fitting stresses to observations

In order to quantify the comparison between modelled stresses and geological observations, we adopt a misfit function (ϕ). Since the observations contain information on both the stress regimes and stress orientations (azimuths) at the observation locations (see Figure 1), we compute the misfits for both (ϕ_{reg} and ϕ_{azi}).

We determine the stress regime using the regime index (R') as defined by (Delvaux et al., 1997):

$$\begin{aligned} R' &= R && \text{when } \sigma_1 \text{ is vertical (normal stress regime)} \\ R' &= 2 - R && \text{when } \sigma_2 \text{ is vertical (transform stress regime)} \\ R' &= 2 + R && \text{when } \sigma_3 \text{ is vertical (reverse stress regime)} \end{aligned} \tag{A1}$$

where σ_1, σ_2 and σ_3 are the principal stresses ordered from most compressive to most tensile and R is the stress ratio:

$$R = \frac{\sigma_2 - \sigma_3}{\sigma_1 - \sigma_3} \tag{A2}$$

For the relation between R' values (ranging from 0 to 3) and the stress regimes, see Figure A1. Because all observations are related to extensional features, we deem modelled tensile stresses at the observation locations to represent good fits. However, stresses that consist of both a tensile and strike-slip component, could also be responsible for reactivation of rift faults. Only if the modelled stresses are pure strike-slip or reverse, reactivation would not be occurring. In the design of the misfit function for the stress regime (ϕ_{reg}), we use an error function as the transition from the pure strike-slip and reverse regimes with a large misfit to the normal regimes with no misfit (Figure A1). For each location i we calculate the misfit, which is of the form:

$$\phi_{reg,i} = \frac{\mathrm{erf}\Big(\, 6\big(\, R' - 1.25\,\big) + 1\,\Big)}{2} \tag{A3}$$

The misfit function for the stress azimuth (σ_{azi}) is constructed in a similar way. The modelled most tensile horizontal stress (S_{Hmin}) is compared to the extension directions of Figure 1, with Δazi being the difference between the two directions. As described in section 2, oblique rifting could have been responsible for the observed extension. We take a conservative estimate of the possible obliquity and regard a Δazi of 45° as the boundary between good fit and misfit (Figure A2). For each location the azimuthal misfit is calculated with:

$$\phi_{azi,i} = \frac{\mathrm{erf}\Big(\, 15\big(\, \frac{\Delta azi - 35}{90}\,\big) + 1\,\Big)}{2} \tag{A4}$$

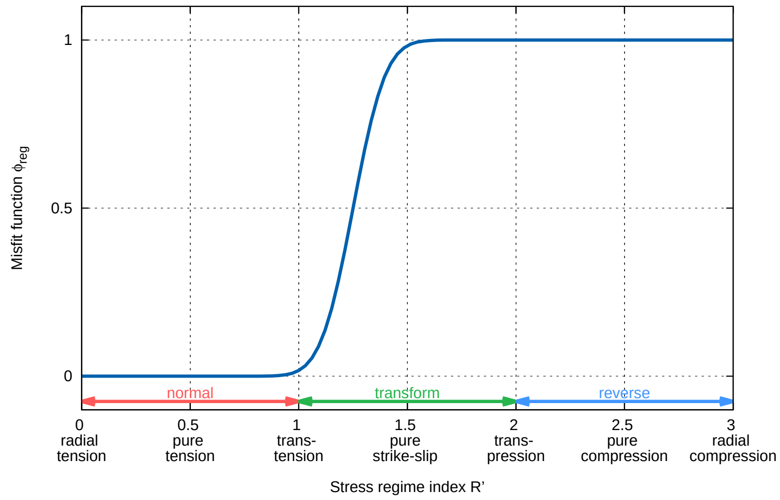

Figure A1. Misfit function for comparing the modelled stress regimes to observations. Stress regimes are calculated following Delvaux et al. (1997).

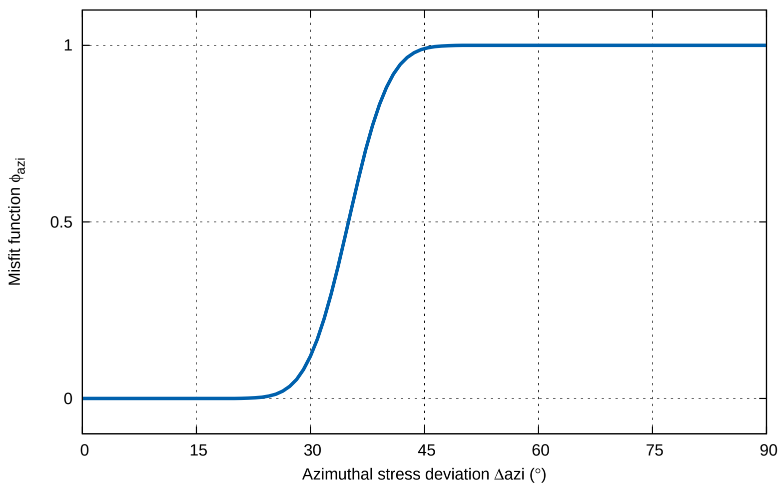

Figure A2. Misfit function for comparing the modelled S_{Hmin} directions to the extension directions of the observations of Figure 1.

For each model the misfits are averaged over the locations and the azimuthal and regime misfits are combined into the single misfit function ϕ:

$$\phi = \frac{\sqrt{\left(\frac{\sum_{i=1}^{N_{obs}} \phi_{reg,i}}{N_{obs}}\right)^2 + \left(\frac{\sum_{i=1}^{N_{obs}} \phi_{azi,i}}{N_{obs}}\right)^2}}{2} \tag{A5}$$

where N_{obs} is the number of observation locations, in our case N_{obs} =8.

Acknowledgments

Author contributions following the CReDiT taxonomy: Conceptualization, M.C.W., L.P.-D., A.T.-M., G.E., J.A. and R.G.; Data curation, M.C.W.; Formal analysis, M.C.W.; Funding acquisition, R.G.; Investigation, M.C.W., L.P.-D., A.T.-M., G.E. and R.G.; Methodology, M.C.W. and R.G.; Project administration, G.E., J.A. and R.G.; Resources, R.G.; Software, M.C.W. and R.G.; Supervision, L.P.-D., G.E., J.A. and R.G.; Validation, M.C.W. and R.G.; Visualization, M.C.W.; Writing - original draft, M.C.W. and R.G.; Writing - review & editing, M.C.W., L.P.-D., A.T.-M., G.E., J.A. and R.G. All map figures were generated using Generic Mapping Tools (Wessel et al., 2013). Input and output files and the software source codes that were used for the models of this paper are digitally stored at Utrecht University. Files are accessible at ftp://ftp.geo.uu.nl/pub/people/govers/2020Tectonics/. MW was partially funded by project NWO DEEP.NL.2018.052. We thank Lukas van der Wiel for his continuous support with the GTECTON numerical model code and Paul Meijer for his comments on an earlier version of this manuscript.

References

Abadi, A. M., van Wees, J. D., van Dijk, P. M., & Cloetingh, S. A. (2008). Tectonics and subsidence evolution of the Sirt Basin, Libya. *AAPG Bulletin*, *92*(8), 993–1027.

Artyushkov, E. V. (1973). Stresses in the Lithosphere Caused by Crustal Thickness Inhomogeneities. *Journal of Geophysical Research*, *78*(32), 7675–7708. doi: 10.1029/jb078i032p07675

Autin, J., Bellahsen, N., Husson, L., Beslier, M. O., Leroy, S., & D'Acremont, E. (2010). Analog models of oblique rifting in a cold lithosphere. *Tectonics*, *29*(6), 1–23. doi: 10.1029/2010TC002671

Ballmer, M. D., Schmerr, N. C., Nakagawa, T., & Ritsema, J. (2015). Compositional mantle layering revealed by slab stagnation at ˜1000-km depth. *Science Advances*, *1*. doi: 10.1126/sciadv.1500815

Barnett-Moore, N., Hassan, R., Müller, R. D., Williams, S. E., & Flament, N. (2017). Dynamic topography and eustasy controlled the paleogeographic evolution of northern Africa since the mid-Cretaceous. *Tectonics*, *36*, 929–944. doi: 10.1002/2016TC004280

Beck, R. A., Burbank, D. W., Sercombe, W. J., Khan, A. M., & Lawrence, R. D. (1996). Late cretaceous ophiolite obduction and paleocene india-asia collision in the westernmost himalaya. *Geodinamica Acta*, *9*(2), 114–144.

Becker, L., Poreda, R. J., Hunt, A. G., Bunch, T. E., & Rampino, M. (2001, 2). Impact Event at the Permian-Triassic Boundary: Evidence from Extraterrestrial Noble Gases in Fullerenes. *Science*, *291*(5508), 1530 LP - 1533.

Behn, M. D., Boettcher, M. S., & Hirth, G. (2007). Thermal structure of oceanic transform faults. *Geology*, *35*(4), 307–310. doi: 10.1130/G23112A.1

Bosworth, W., Guiraud, R., & Kessler, L. G. (1999). Late Cretaceous (ca. 84 Ma) compressive deformation of the stable platform of northeast Africa (Egypt): Far-field stress effects of the "Santonian event" and origin of the Syrian arc deformation belt. *Geology*, *27*(7), 633–636. doi: 10.1130/0091-7613(1999)027⟨0633:LCCMCD⟩2.3.CO;2

Bosworth, W., & Morley, C. K. (1994). Structural and stratigraphic evolution of the Anza rift, Kenya. *Tectonophysics*, *236*, 93–115. doi: 10.1016/0040-1951(94)90171-6

Bosworth, W., & Stockli, D. F. (2016). Early magmatism in the greater Red Sea rift: timing and significance. *Canadian Journal of Earth Sciences*, *53*, 1158–1176. doi: 10.1139/cjes-2016-0019

Brew, G., Best, J., Barazangi, M., & Sawaf, T. (2003). Tectonic evolution of the NE Palmyride mountain belt, Syria: the Bishri crustal block. *Journal of the Geological Society*, *160*, 677–685. doi: 10.1144/0016-764902-161

Burkett, E. R., & Billen, M. I. (2010). Three-dimensionality of slab detachment due to ridge-trench collision: Laterally simultaneous boudinage versus tear propagation. *Geochemistry, Geophysics, Geosystems*, *11*(11). doi: 10.1029/2010GC003286

Byerlee, J. (1978). Friction of rocks. In *Rock friction and earthquake prediction* (pp. 615–626). Springer. doi: 10.1007/BF00876528

Capitanio, F. A., Morra, G., & Goes, S. (2009). Dynamics of plate bending at the trench and slab-plate coupling. *Geochemistry, Geophysics, Geosystems*, *10*(4). doi: 10.1029/2008GC002348

Capitanio, F. A., Morra, G., Goes, S., Weinberg, R. F., & Moresi, L. (2010). India-Asia convergence driven by the subduction of the Greater Indian continent. *Nature Geoscience*, *3*(2), 136–139. doi: 10.1038/ngeo725

Chapple, W. M., & Tullis, T. E. (1977). Evaluation of the forces that drive the plates. *Journal of Geophysical Research*, *82*(14), 1967–1984.

Čížková, H., van den Berg, A. P., Spakman, W., & Matyska, C. (2012). The viscosity of Earth's lower mantle inferred from sinking speed of subducted lithosphere. *Physics of the Earth and Planetary Interiors*, *200*, 56–62.

Cloetingh, S., & Burov, E. (2011). Lithospheric folding and sedimentary basin evolution: A review and analysis of formation mechanisms. *Basin Research*, *23*(3), 257–290. doi: 10.1111/j.1365-2117.2010.00490.x

Coblentz, D. D., & Richardson, R. M. (1996). Analysis of the South American intraplate stress field. *Journal of Geophysical Research*, *101*(B4), 8643–8657. doi: 10.1029/96jb00090

Coblentz, D. D., Sandiford, M., Richardson, R. M., Zhou, S., & Hillis, R. (1995). The origins of the intraplate stress field in continental Australia. *Earth and Planetary Science Letters*, *133*, 299–309. doi: 10.1016/0012-821X(95)00084-P

Coblentz, D. D., Zhou, S., Hillis, R. R., Richardson, R. M., & Sandiford, M. (1998). Topography, boundary forces, and the Indo-Australian intraplate stress field. *Journal of Geophysical Research*, *103*(B1), 919–931.

Conrad, C. P., Bilek, S., & Lithgow-Bertelloni, C. (2004). Great earthquakes and slab pull: Interaction between seismic coupling and plate-slab coupling. *Earth and Planetary Science Letters*, *218*, 109–122. doi: 10.1016/S0012-821X(03)00643-5

Conrad, C. P., & Lithgow-Bertelloni, C. (2002). How Mantle Slabs Drive Plate Motions. *Science*, *298*, 207–210. doi: 10.1126/science.1074161

Conrad, C. P., & Lithgow-Bertelloni, C. (2006). Influence of continental roots and asthenosphere on plate-mantle coupling. *Geophysical Research Letters*, *33*(5), 2–5. doi: 10.1029/2005GL025621

Copley, A., Avouac, J. P., & Royer, J. Y. (2010). India-Asia collision and the Cenozoic slowdown of the Indian plate: Implications for the forces driving plate motions. *Journal of Geophysical Research: Solid Earth*, *115*(3), 1–14. doi: 10.1029/2009JB006634

Corfield, R. I., Searle, M. P., & Pedersen, R. B. (2001). Tectonic Setting, Origin, and Obduction History of the Spontang Ophiolite, Ladakh Himalaya, NW India. *The Journal of Geology*, *109*, 715–736. doi: 10.1086/323191

Cowie, L., & Kusznir, N. (2018). Renormalisation of global mantle dynamic topography predictions using residual topography measurements for "normal" oceanic crust. *Earth and Planetary Science Letters*, *499*, 145–156. doi: 10.1016/j.epsl.2018.07.018

Davies, D. R., Valentine, A. P., Kramer, S. C., Rawlinson, N., Hoggard, M. J., Eakin, C. M., & Wilson, C. R. (2019). Earth's multi-scale topographic response to global mantle flow. *Nature Geoscience*, *12*(10), 845–850. doi: 10.1038/s41561-019-0441-4

Delvaux, D., Moeys, R., Stapel, G., Petite, C., Levi, K., Miroshnichenko, A., ... San'kov, V. (1997). Paleostress reconstructions and geodynamics of the Baikal region, Central Asia, Part 2. Cenozoic rifting. *Tectonophysics*, *282*, 1–38.

Doubrovine, P. V., Steinberger, B., & Torsvik, T. H. (2012). Absolute plate motions in a reference frame defined by moving hot spots in the Pacific, Atlantic, and Indian oceans. *Journal of Geophysical Research*, *117*, 1–30. doi: 10.1029/2011JB009072

England, P., & Wortel, R. (1980). Some consequences of the subduction of young slabs. *Earth and Planetary Science Letters*, *47*, 403–415. doi: 10.1016/0012-821X(80)90028-X

Flament, N., Gurnis, M., & Müller, R. D. (2013). A review of observations and models of dynamic topography. *Lithosphere*, *5*(2), 189–210.

Fleitout, L., & Froidevaux, C. (1982). Tectonics and topography for a lithosphere containing density heterogeneities. *Tectonics*, *1*(1), 21–56.

Forsyth, D., & Uyeda, S. (1975). On the Relative Importance of the Driving forces of Plate Motion. *Geophysical Journal of the Royal Astronomical Society*, *43*, 163–200. doi: 10.1111/j.1365-246X.1975.tb04143.x

Fournier, M., Chamot-Rooke, N., Rodriguez, M., Huchon, P., Petit, C., Beslier, M. O., & Zaragosi, S. (2011). Owen Fracture Zone: The Arabia-India plate boundary unveiled. *Earth and Planetary Science Letters*, *302*, 247–252. doi: 10.1016/j.epsl.2010.12.027

Frank, F. C. (1972). Plate tectonics, the analogy with glacier flow, and isostasy. *Geophysical Monograph Series: Flow and Fracture of Rocks*, *16*, 285–292.

Fukao, Y., & Obayashi, M. (2013). Subducted slabs stagnant above, penetrating through, and trapped below the 660 km discontinuity. *Journal of Geophysical Research: Solid Earth*, *118*, 5920–5938. doi: 10.1002/2013JB010466

Fukao, Y., Obayashi, M., Nakakuki, T., & the Deep Slab Project Group. (2009). Stagnant Slab: A Review. *Annual Review of Earth and Planetary Sciences*, *37*, 19–46. doi: 10.1146/annurev.earth.36.031207.124224

Gaina, C., Torsvik, T. H., van Hinsbergen, D. J., Medvedev, S., Werner, S. C., & Labails, C. (2013). The African plate: A history of oceanic crust accretion and subduction since the Jurassic. *Tectonophysics*, *604*, 4–25.

Globig, J., Fernàndez, M., Torne, M., Vergés, J., Robert, A., & Faccenna, C. (2016). New insights into the crust and lithospheric mantle structure of Africa from elevation, geoid, and thermal analysis. *Journal of Geophysical Research-Solid Earth*, *121*, 5389–5424.

Goes, S., Capitanio, F. A., Morra, G., Seton, M., & Giardini, D. (2011). Signatures of downgoing plate-buoyancy driven subduction in Cenozoic plate motions. *Physics of the Earth and Planetary Interiors*, *184*, 1–13. doi: 10.1016/j.pepi.2010.10.007

Gordon, R. G., & Demets, C. (1989). Present-day motion along the Owen fracture zone and Dalrymple trough in the Arabian Sea. *Journal of Geophysical Research*, *94*(B5), 5560–5570. doi: 10.1029/JB094iB05p05560

Govers, R., & Meijer, P. T. (2001). On the dynamics of the Juan de Fuca plate. *Earth and Planetary Science Letters*, *189*, 115–131.

Guiraud, R., & Bosworth, W. (1997). Senonian basin inversion and rejuvenation of rifting in Africa and Arabia: synthesis and implications to plate-scale tectonics. *Tectonophysics*, *282*, 39–82. doi: 10.1016/S0040-1951(97)00212-6

Guiraud, R., Bosworth, W., Thierry, J., & Delplanque, A. (2005). Phanerozoic geological evolution of Northern and Central Africa : An overview. *Journal of African Earth Sciences*, *43*, 83–143. doi: 10.1016/j.jafrearsci.2005.07.017

Heidbach, O., Rajabi, M., Reiter, K., Ziegler, M., & the WSM team. (2016). World Stress Map Database Release. *GFZ Data Services*.

Heidbach, O., Tingay, M., Barth, A., Reinecker, J., Kurfeß, D., & Müller, B. (2010). Global crustal stress pattern based on the World Stress Map database release 2008. *Tectonophysics*, *482*, 3–15.

Hoggard, M. J., White, N., & Al-Attar, D. (2016). Global dynamic topography observations reveal limited influence of large-scale mantle flow. *Nature Geoscience*, *9*, 456–463. doi: 10.1038/ngeo2709

Humphreys, E. D., & Coblentz, D. D. (2007). North American dynamics and western U.S. tectonics. *Reviews of Geophysics*, *45*(RG3001), 1–30.

Ito, E., & Sato, H. (1991). Aseismicity in the lower mantle by superplasticity of the descending slab. *Nature*, *351*, 140–141. doi: 10.1038/351140a0

Janssen, M. E., Stephenson, R. A., & Cloetingh, S. (1995). Temporal and spatial correlations between changes in plate motions and the evolution of rifted basins in Africa. *Geological Society of America Bulletin*, *107*(11), 1317–1332. doi: 10.1130/0016-7606(1995)107⟨1317:TASCBC⟩2.3.CO;2

King, S. D. (2016a). An evolving view of transition zone and midmantle viscosity. *Geochemistry, Geophysics, Geosystems*, *17*, 1234–1237. doi: 10.1002/2016GC006279

King, S. D. (2016b). Reconciling laboratory and observational models of mantle rheology in geodynamic modelling. *Journal of Geodynamics*, *100*, 33–50. doi: 10.1016/j.jog.2016.03.005

King, S. D., Frost, D. J., & Rubie, D. C. (2015). Why cold slabs stagnate in the transition zone. *Geology*, *43*(3), 231–234. doi: 10.1130/G36320.1

Kohlstedt, D., Evans, B., & Mackwell, S. (1995). Strength of the lithosphere: Constraints imposed by laboratory experiments. *Journal of Geophysical Research*, *100*(B9), 17587–17602. doi: 10.1029/95JB01460

Lallemand, S., Heuret, A., & Boutelier, D. (2005). On the relationships between slab dip, back-arc stress, upper plate absolute motion, and crustal nature in subduction zones. *Geochemistry, Geophysics, Geosystems*, *6*(9).

Laske, G., Masters, G., Ma, Z., & Pasyanos, M. E. (2013). Update on CRUST1.0 - A 1-degree Global Model of Earth's Crust. *EGU General Assembly*, *15*, 2658.

McClay, K. R., & White, M. J. (1995). Analogue modelling of orthogonal and oblique rifting. *Marine and Petroleum Geology*, *12*(2), 137–151. doi: 10.1016/0264-8172(95)92835-K

Meijer, P. T., & Wortel, M. J. R. (1992). The dynamics of motion of the South American Plate. *Journal of Geophysical Research*, *97*(B8), 11915–11931.

Meijer, P. T., & Wortel, M. J. R. (1997). Present-day dynamics of the Aegean region : A model analysis of the horizontal pattern of stress and deformation. *Tectonics*, *16*(6), 879–895.

Meijer, P. T., & Wortel, M. J. R. (1999). Cenozoic dynamics of the African plate with emphasis on the Africa-Eurasia collision. *Journal of Geophysical Research-Solid Earth*, *104*(B4), 7405–7418. doi: 10.1029/1999jb900009

Molnar, P., England, P. C., & Jones, C. H. (2015). Mantle dynamics, isostasy, and the support of high terrain. *Journal of Geophysical Research : Solid Earth*, *120*, 1932–1957.

Moucha, R., & Forte, A. M. (2011). Changes in African topography driven by mantle convection. *Nature Geoscience*, *4*(10), 707–712. doi: 10.1038/ngeo1235

Müller, R. D., Hassan, R., Gurnis, M., Flament, N., & Williams, S. E. (2018). Dynamic topography of passive continental margins and their hinterlands since the Cretaceous. *Gondwana Research*, *53*, 225–251. doi: 10.1016/j.gr.2017.04.028

Nijholt, N. (2019). *STEP faults and lithosphere dynamics in the Mediterranean* (Doctoral dissertation, Utrecht University). Retrieved from `https://dspace.library.uu.nl/handle/1874/386073`

Nijholt, N., Govers, R., & Wortel, R. (2018). On the forces that drive and resist deformation of the south-central Mediterranean: A mechanical model study. *Geophysical Journal International*, *214*, 876–894.

Pallares, C., Maury, R. C., Bellon, H., Royer, J.-Y., Calmus, T., Aguillón-Robles, A., ... Bourgois, J. (2007). Slab-tearing following ridge-trench collision: Evidence from Miocene volcanism in Baja California, México. *Journal of Volcanology and Geothermal Research*, *161*, 95–117. doi: 10.1016/j.jvolgeores.2006.11.002

Pérez-Díaz, L., & Eagles, G. (2014). Constraining South Atlantic growth with seafloor spreading data. *Tectonics*, *33*(9), 1848–1873. doi: 10.1002/2014TC003644

Pérez-Díaz, L., & Eagles, G. (2017). A new high-resolution seafloor age grid for the South Atlantic. *Geochemistry Geophysics Geosystems*, *18*, 457–470.

Phillips, B. R., & Bunge, H. P. (2005). Heterogeneity and time dependence in 3D spherical mantle convection models with continental drift. *Earth and Planetary Science Letters*, *233*, 121–135. doi: 10.1016/j.epsl.2005.01.041

Quinteros, J., Sobolev, S. V., & Popov, A. A. (2010). Viscosity in transition zone and lower mantle: Implications for slab penetration. *Geophysical Research Letters*, *37*(9). doi: 10.1029/2010gl043140

Rey, P., Vanderhaeghe, O., & Teyssier, C. (2001). Gravitational collapse of the continental crust: definition, regimes and modes. *Tectonophysics*, *342*, 435–449. doi: 10.1016/S0040-1951(01)00174-3

Richardson, R. M., & Reding, L. M. (1991). North American Plate Dynamics. *Journal of Geophysical Research*, *96*(B7), 12201–12223. doi: 10.1029/91jb00958

Richter, F., & McKenzie, D. (1978). Simple Plate Models of Mantle Convection. *Journal of Geophysics*, *44*, 441 - 471.

Sandiford, M., & Coblentz, D. (1994). Plate-scale potential-energy distributions and the fragmentation of ageing plates. *Earth and Planetary Science Letters*, *126*, 143–159.

Schellart, W. P. (2004). Quantifying the net slab pull force as a driving mechanism for plate tectonics. *Geophysical Research Letters*, *31*(7), 10–14. doi: 10.1029/2004GL019528

Seton, M., Müller, R. D., Zahirovic, S., Gaina, C., Torsvik, T., Shephard, G., ... Chandler, M. (2012). Global continental and ocean basin reconstructions since 200 Ma. *Earth-Science Reviews*, *113*, 212–270.

Spasojevic, S., & Gurnis, M. (2012). Sea level and vertical motion of continents from dynamic earth models since the late cretaceous. *AAPG Bulletin*, *96*(11), 2037–2064. doi: 10.1306/03261211121

Stampfli, G. M., & Borel, G. D. (2004). The TRANSMED Transects in Space and Time: Constraints on the Paleotectonic Evolution of the Mediterranean Domain. In *The transmed atlas. the mediterranean region from crust to mantle* (pp. 53–81). Springer Berlin Heidelberg. doi: 10.1007/978-3-642-18919-7

Stampfli, G. M., Borel, G. D., Marchant, R., & Mosar, J. (2002). Western Alps geological constraints on western Tethyan reconstructions. *Journal of the Virtual Explorer*, *8*, 77–106.

Stamps, D. S., Iaffaldano, G., & Calais, E. (2015). Role of mantle flow in Nubia-Somalia plate divergence. *Geophysical Research Letters*, *42*(2), 290–296. doi: 10.1002/2014GL062515

Stefanick, M., & Jurdy, M. (1992). Stress Observations and Driving Force Models for the South American plate. *Journal of Geophysical Research*, *97*(B8), 11905–11913.

Stein, C. A., & Stein, S. (1992). A model for the global variation in oceanic depth and heat flow with lithospheric age. *Nature*, *359*, 123–129.

Steinberger, B., & Becker, T. W. (2018, 10). A comparison of lithospheric thickness models. *Tectonophysics*, *746*, 325–338. doi: 10.1016/j.tecto.2016.08.001

Stotz, I. L., Iaffaldano, G., & Davies, D. R. (2017). Late Miocene Pacific plate kinematic change explained with coupled global models of mantle and lithosphere dynamics. *Geophysical Research Letters*, *44*(14), 7177–7186. doi: 10.1002/2017GL073920

Stotz, I. L., Iaffaldano, G., & Davies, D. R. (2018). Pressure-Driven Poiseuille Flow: A Major Component of the Torque-Balance Governing Pacific Plate Motion. *Geophysical Research Letters*, *45*, 117–125. doi: 10.1002/2017GL075697

Torsvik, T. H., Müller, R. D., Voo, R. V. D., Steinberger, B., & Gaina, C. (2008). Global plate motion frames: toward a unified model. *Reviews of Geophysics*, *46*, 1–44.

Tuck-Martin, A., Adam, J., & Eagles, G. (2018). New plate kinematic model and tectono-stratigraphic history of the East African and West Madagascan Margins. *Basin Research*, *30*(6), 1118–1140.

Van Benthem, S., & Govers, R. (2010). The Caribbean plate: Pulled, pushed, or dragged? *Journal of Geophysical Research*, *115*(B10409), 1–14.

Van Der Voo, R., Spakman, W., & Bijwaard, H. (1999). Tethyan subducted slabs under India. *Earth and Planetary Science Letters*, *171*, 7–20. doi: 10.1016/S0012-821X(99)00131-4

Van Hinsbergen, D., Torsvik, T. H., Schmid, S. M., Matenco, L. C., Maffione, M., Vissers, R. L., … Spakman, W. (2019). Orogenic architecture of the Mediterranean region and kinematic reconstruction of its tectonic evolution since the Triassic. *Gondwana Research*, *81*, 79–229. doi: 10.1016/j.gr.2019.07.009

van Hinsbergen, D. J. J., Hafkenscheid, E., Spakman, W., Meulenkamp, J. E., & Wortel, R. (2005). Nappe stacking resulting from subduction of oceanic and continental lithosphere below Greece. *Geology*, *33*(4), 325–328. doi: 10.1130/G20878.1

Van Summeren, J., Conrad, C. P., & Lithgow-Bertelloni, C. (2012). The importance of slab pull and a global asthenosphere to plate motions. *Geochemistry, Geophysics, Geosystems*, *13*(1). doi: 10.1029/2011GC003873

Viola, G., Kounov, A., Andreoli, M. A., & Mattila, J. (2012). Brittle tectonic evolution along the western margin of South Africa: More than 500 Myr of continued reactivation. *Tectonophysics*, *514-517*, 93–114.

Warners-Ruckstuhl, K. N., Govers, R., & Wortel, R. (2012). Lithosphere-mantle coupling and the dynamics of the Eurasian Plate. *Geophysical Journal International*, *189*, 1253–1276. doi: 10.1111/j.1365-246X.2012.05427.x

Warners-Ruckstuhl, K. N., Govers, R., & Wortel, R. (2013). Tethyan collision forces and the stress field of the Eurasian Plate. *Geophysical Journal International*, *195*, 1–15. doi: 10.1093/gji/ggt219

Warners-Ruckstuhl, K. N., Meijer, P. T., Govers, R., & Wortel, M. J. R. (2010). A lithosphere-dynamics constraint on mantle flow: Analysis of the Eurasian plate. *Geophysical Research Letters*, *37*(18), 1–6.

Weatherall, P., Marks, K. M., Jakobsson, M., Schmitt, T., Tani, S., Arndt, J. E., … Wigley, R. (2015). A new digital bathymetric model of the world's oceans. *Earth and Space Science*, *2*, 331–345. doi: 10.1002/2015EA000107.Received

Wessel, P., Smith, W. H., Scharroo, R., Luis, J., & Wobbe, F. (2013). Generic mapping tools: Improved version released. *Eos*, *94*(45), 409–410. doi: 10.1002/2013EO450001

Williams, S., Flament, N., Dietmar Müller, R., & Butterworth, N. (2015). Absolute plate motions since 130 Ma constrained by subduction zone kinematics. *Earth and Planetary Science Letters*, *418*, 66–77. doi: 10.1016/j.epsl.2015.02.026

Wortel, M. J. R., & Cloetingh, S. (1981). On the origin of the Cocos-Nazca spreading center. *Geology*, *9*(9), 425–430.

Wortel, M. J. R., Remkes, M. J. N., Govers, R., Cloetingh, S. A. P. L., & Meijer,

P. T. (1991). Dynamics of the lithosphere and the intraplate stress field. *Philosophical Transactions of the Royal Society of London A*, *337*(1645), 111–126.

Wortel, M. J. R., & Spakman, W. (2000). Subduction and slab detachment in the Mediterranean-Carpathian region. *Science*, *290*(5498), 1910–1917. doi: 10.1126/science.290.5498.1910

Xie, X., & Heller, P. L. (2009). Plate tectonics and basin subsidence history. *Bulletin of the Geological Society of America*, *121*(1-2), 55–64. doi: 10.1130/B26398.1

Zoback, M. D., Stephenson, R. A., Cloetingh, S., Larsen, B. T., Van Hoorn, B., Robinson, A., … Ben-Avraham, Z. (1993). Stresses in the lithosphere and sedimentary basin formation. *Tectonophysics*, *226*, 1–13. doi: 10.1016/0040-1951(93)90107-U

Zoback, M. L. (1992). First- and second-order patterns of stress in the lithosphere: The World Stress Map Project. *Journal of Geophysical Research*, *97*(B8), 11703–11728. doi: 10.1029/92jb00132